Intraseasonal Variability of SST and Precipitation in the Arabian Sea during the Indian Summer Monsoon: Impact of Ocean Mixed Layer Depth

YUANLONG LI AND WEIQING HAN

Department of Atmospheric and Oceanic Sciences, University of Colorado Boulder, Boulder, Colorado

WANQIU WANG

Climate Prediction Center, NOAA/NWS/NCEP, College Park, Maryland

M. RAVICHANDRAN

Indian National Centre for Ocean Information Services, Hyderabad, Andhra Pradesh, India

(Manuscript received 22 March 2016, in final form 16 June 2016)

ABSTRACT

This study investigates sea surface temperature (SST) and precipitation variations in the eastern Arabian Sea (EAS) induced by the northward-propagating Indian summer monsoon (ISM) intraseasonal oscillations (MISOs) through analyzing satellite observations and the Climate Forecast System Reanalysis (CFSR) and performing ocean general circulation model (OGCM) experiments. MISOs in the EAS achieve the largest intensity in the developing stage (May–June) of the ISM. The MISOs induce intraseasonal SST variability primarily through surface heat flux forcing, contributed by both shortwave radiation and turbulent heat flux, and secondarily through mixed layer entrainment. The shallow mixed layer depth (MLD < 40 m) in the developing stage and decaying stage (September–October) of the ISM significantly amplifies the heat flux forcing effect on SST and causes large intraseasonal SST variability. Meanwhile, the high SST (>29°C) in the developing stage leads to enhanced response of MISO convection to SST anomaly. It means that the ocean state of the EAS region during the developing stage favors active two-way air–sea interaction and the formation of the strong first-pulse MISO event. These results provide compelling evidence for the vital role played by the ocean in the MISO mechanisms and have implications for understanding and forecasting the ISM onset. Compared to satellite observation, MISOs in CFSR data have weaker SST variability by ~50% and biased SST–precipitation relation. Reducing these biases in CFSR, which provides initial conditions of the National Centers for Environmental Prediction (NCEP) Climate Forecast System version 2 (CFSv2), may help improve the ISM rainfall forecast.

1. Introduction

During boreal summer, the north Indian Ocean is dominated by prevailing southwesterly winds and heavy rainfall (Fig. 1), characterizing the Indian summer monsoon (ISM). The ISM, as a major component of the Asian monsoon system, has profound impacts on the agriculture, economy, and environment of South and Southeast Asian countries (e.g., Gadgil and Rupa Kumar 2006). Accurate prediction of the ISM rainfall is of paramount importance for agriculture planning and society adaptation and therefore a major task for climate researchers. The ISM system, however, exhibits strong and complicated variability over a wide range of time scales, which makes its simulation and prediction rather challenging for climate models (e.g., Wang et al. 2005; Goswami et al. 2006; Goswami et al. 2015). One substantial component of the ISM rainfall variability is at the intraseasonal time scale, which typically manifests as fluctuations between active spells with good rainfall and break spells with little rainfall over India (Goswami and Ajaya Mohan 2001; Webster et al. 2002; Rajeevan et al. 2010). Prolonged or frequent breaks can cause widespread drying over South Asia and lead to substantial agricultural yield reduction. The active and break spells are closely associated with the

Corresponding author address: Yuanlong Li, Department of Atmospheric and Oceanic Sciences, University of Colorado Boulder, Campus Box 311, Boulder, CO 80309.
E-mail: yuanlong.li@colorado.edu

DOI: 10.1175/JCLI-D-16-0238.1

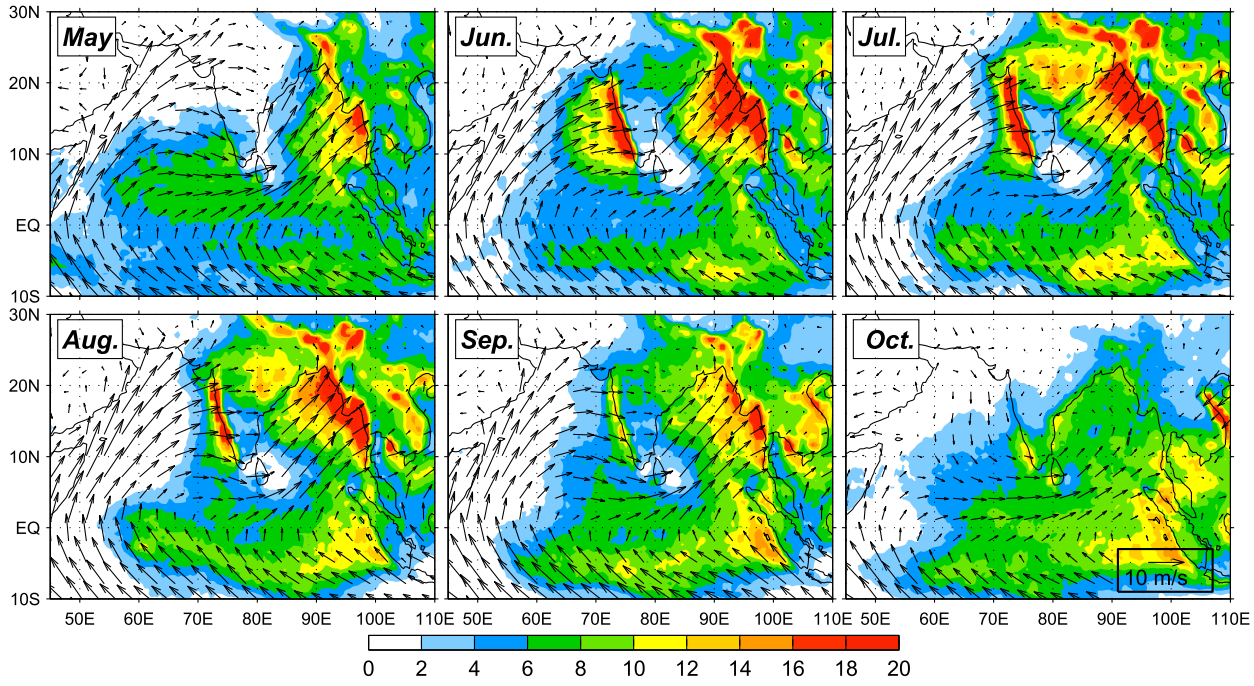

FIG. 1. Monthly climatology of precipitation (color shading; mm day^{-1}) and 10-m winds (vectors; m s^{-1}) for May–October based on TRMM and CCMP data of 1998–2011.

large-scale atmospheric intraseasonal oscillations, referred to as the monsoon intraseasonal oscillations (MISOs; Yasunari 1979, 1980). The ISM rainfall shows two spectral peaks within the intraseasonal band, corresponding to the two dominant modes of the MISO. The low-frequency mode has a typical period of 30–60 days and propagates northward/northeastward from the equatorial Indian Ocean to South Asia. Some of them are associated with the eastward-propagating Madden–Julian oscillations along the equator (e.g., Madden and Julian 1971; Lau and Chan 1985; Zhang 2005). The 10–20-day high-frequency mode is the manifestation of convectively coupled Kelvin and Rossby waves and propagates westward/northwestward from the western Pacific Ocean (e.g., Krishnamurti and Ardanuy 1980; Kiladis and Weickmann 1997; Chatterjee and Goswami 2004). These MISOs affect not only the onset/withdrawal and active/break spells of the ISM but also the seasonal evolution and interannual variability of the monsoon precipitation (e.g., Lau and Chan 1985; Annamalai and Slingo 2001; Hoyos and Webster 2007).

Many mechanisms have been proposed to understand the MISO dynamics. At the lowest order the MISO is considered as an internal instability mode of the tropical atmosphere (e.g., Wang and Xie 1998; Lawrence and Webster 2002; Jiang et al. 2004; Drbohlav and Wang 2005). For example, Jiang et al. (2004) suggest that the northward-propagating 30–60-day MISOs arise from the convection–moisture feedback associated with moisture advection of low-level winds. According to Jiang et al.'s (2004) theory, the vertical shear of monsoon winds can result in positive vorticity and moisture convergence to the north of the convection center, leading to the northward shift of the convection system. On the other hand, air–sea interaction has been shown to play an important role in MISO dynamics (e.g., Kemball-Cook and Wang 2001; Fu et al. 2002, 2003; Roxy and Tanimoto 2007). Many observational studies have described coherent variations in sea surface temperature (SST) and atmospheric fields during MISO events in the tropical Indian Ocean (Sengupta and Ravichandran 2001; Sengupta et al. 2001; Harrison and Vecchi 2001; Joseph and Sabin 2008), and air–sea interaction is suggested to be important in their northward propagation. The warm SST to the north of the convection center can destabilize the lower atmosphere and lead to the northward movement of the convection system (Kemball-Cook and Wang 2001; Harrison and Vecchi 2001; Roxy and Tanimoto 2007). The importance of air–sea interaction, especially the SST feedbacks to the atmosphere, in the MISO dynamics has been confirmed by modeling studies (Fu et al. 2002, 2003; Fu and Wang 2004; Rajendran and Kitoh 2006; Seo et al. 2007; Wang et al. 2009; Achuthavarier and Krishnamurthy 2011). Intraseasonal SST anomalies over the tropical Indian Ocean can dramatically modify the simulated MISOs in amplitude,

frequency, and propagation behaviors. By considering intraseasonal air–sea interaction, coupled general circulation models (GCMs) produce more realistic MISOs in spatiotemporal characteristics and SST–precipitation relationship than SST-forced atmosphere GCMs (e.g., Fu et al. 2003; Pegion and Kirtman 2008; Seo et al. 2007; Wang et al. 2009; Sharmila et al. 2013) and significantly extend the predictability of the ISM rainfall (Waliser et al. 2001; Fu et al. 2007, 2008). Consequently, investigating the intraseasonal Indian Ocean SST variability and its feedback to the atmosphere will help to further understand the MISO dynamics and improve ISM rainfall prediction.

The ISM onset starts in the Western Ghats (Sahyadri) of India during May–June (e.g., Joseph et al. 1994; Webster et al. 1998; Wu and Wang 2001), often triggered by the first strong MISO event of the year (e.g., Lau and Yang 1996; K. Li et al. 2013; Zhou and Murtugudde 2014). MISOs induce prominent SST variability in the Arabian Sea, Bay of Bengal (BoB), eastern equatorial Indian Ocean Basin, and South China Sea (e.g., Sengupta et al. 2001; Harrison and Vecchi 2001; Joseph and Sabin 2008; Duncan and Han 2009; Roxy and Tanimoto 2012). Among others, SST in the Arabian Sea is of particular interest because of its vital impact on the onset and variability of the ISM (e.g., Shukla 1975; Rao and Sivakumar 1999; Izumo et al. 2008; Prodhomme et al. 2015). The mini warm pool of the Arabian Sea formed in spring is the primary moisture source for the ISM rainfall (Ninomiya and Kobayashi 1999). Positive SST anomalies over the eastern Arabian Sea (EAS) tend to occur prior to the positive precipitation anomalies of MISOs and provide a favorable condition for convective activity (Roxy and Tanimoto 2007). Xi et al. (2015) found that intraseasonal SST anomalies in the EAS contribute to the atmospheric static instability and deep convection of MISOs. Roxy et al. (2013) showed that the response of precipitation to intraseasonal SST anomaly is much faster in the EAS (~5 days) than in the BoB and South China Sea (~12 days), indicative of a more active role of the ocean in MISO mechanisms. Intraseasonal SST variability and relevant upper-ocean processes in the Arabian Sea deserve more attention from the climate community. For example, the ocean mixed layer depth (MLD) is a crucial factor in determining intraseasonal SST amplitude (e.g., Keerthi et al. 2013; Roxy et al. 2013; Li et al. 2014). A shallow (deep) MLD can amplify (attenuate) the SST response to atmospheric forcing of the MISO. Roxy et al. (2013) suggested that the systematic bias of the modeled MLD is a primary error source for the MISO simulation of the National Centers for Environmental Prediction (NCEP) Climate Forecast System version 2 (CFSv2; Saha et al. 2014).

The present study is mainly motivated by three objectives. First, we aim to provide a comprehensive description of the intraseasonal SST and precipitation variability during the ISM, underscoring its unique characteristics in the Arabian Sea. We analyze recent high-quality satellite observations and the NCEP Climate Forecast System Reanalysis (CFSR) data, which are used to initialize the CFSv2 forecast. Given the importance of the initial condition in the extended-range forecast of the ISM (Goswami and Gouda 2009; Abhilash et al. 2014; Alessandri et al. 2015), evaluating CFSR in representing MISOs and air–sea interaction processes may provide implications for improving the CFSv2 monsoon forecast. Second, we attempt to gain insights into the upper-ocean processes controlling intraseasonal SST variability in the Arabian Sea. This is pursued through ocean GCM (OGCM) experiments that can isolate effects of different forcing on SST and a mixed layer heat budget analysis using the OGCM results. Finally, we examine the impact of the ocean state, such as MLD, on intraseasonal SST variability and MISOs. Through these efforts, the present study will complement our knowledge of air–sea interaction processes involved in MISO dynamics and thereby help to identify the targets for improving CFSv2 monsoon forecast. The rest of the paper is organized as follows. Section 2 outlines the satellite observational data, reanalysis data, and the OGCM utilized in this study. Section 3 describes the characteristics of intraseasonal SST and precipitation variability associated with MISOs from observational data and CFSR. Section 4 explores oceanic processes controlling intraseasonal SST variability in the EAS and examines the impact of MLD. Finally, section 5 summarizes the main results and provides discussion.

2. Data and model

a. Observational data

In this study we analyze high-quality satellite observations during 1998–2014. For precipitation, we use the Tropical Rainfall Measuring Mission (TRMM) Multisatellite Precipitation Analysis (TMPA) level 3B42 version 7 (V7) product (Huffman et al. 2007). It provides calibrated daily precipitation estimates from multiple satellites and gauge analyses with 0.25° × 0.25° spatial resolution. For SST, we use the TRMM Microwave Imager (TMI) V7 product (Wentz et al. 2000), which provides 0.25° × 0.25°, 3-day running mean, daily SST fields based on satellite microwave measurements. We also use the geostationary enhanced 1° × 1° shortwave and longwave radiation (SWR and LWR) products of Clouds and the Earth's Radiant Energy System (CERES; Wielicki et al. 1996; Loeb et al. 2001) available since March 2000. Daily

turbulent heat flux Q_T (latent heat flux plus sensible heat flux) with 1° × 1° resolution is taken from the objectively analyzed air–sea fluxes (OAFlux; Yu and Weller 2007), and daily 0.25° × 0.25° surface winds are from the cross-calibrated multiplatform (CCMP) ocean 10-m wind vectors (Atlas et al. 2008) during 1998–2011. In addition, the 1° × 1° monthly ocean temperature and salinity data during 2001–14 from the gridpoint value of the monthly objective analysis using the Argo data (MOAA GPV; Hosoda et al. 2008) are used for estimating the observational MLD.

In this study intraseasonal variations associated with MISOs are represented by 20–90-day anomalies of oceanic and atmospheric variables in the tropical Indian Ocean. They are obtained by first removing the mean seasonal cycle and then applying a Lanczos bandpass filter (Duchon 1979). The 20–90-day fluctuations are primarily signatures of the 30–60-day mode of the MISO propagating northward from the equatorial Indian Ocean to South Asia. The northwestward-propagating 10–20-day mode is therefore out of the scope of the present research.

b. CFSR

We also analyze precipitation, SST, winds, heat fluxes, and MLD of the CFSR data (Saha et al. 2010; Xue et al. 2011) developed by NCEP. The CFSR data spanning January 1998–December 2010 are downloaded from the National Oceanic and Atmospheric Administration (NOAA) national operational model archive and distribution system (NOMADS) and the National Center for Atmospheric Research (NCAR) in hourly resolution and averaged into daily data. Comparing with earlier versions of NCEP reanalysis products and other widely used atmospheric reanalysis data, CFSR has many advantages (Saha et al. 2010; Wang et al. 2011). First, it is the first reanalysis system in which the guess fields are 6-hourly forecast results of a coupled atmosphere–ocean-ice climate system. Second, it uses higher horizontal (~38 km) and vertical (64 levels) resolutions in the atmosphere component. Third, it assimilates satellite-based radiances rather than the retrieved temperature and humidity values. The ocean component of CFSR is the Geophysical Fluid Dynamics Laboratory (GFDL) Modular Ocean Model version 4.0 (MOM4) with a zonal resolution of 0.5° and a meridional resolution changing gradually from 0.25° between 10°S and 10°N to 0.5° poleward of 30°S and 30°N. The top-layer thickness of MOM4 is 10 m, and therefore SST of CFSR in fact represents the bulk temperature of 0–10 m. Satellite and in situ ocean observations are assimilated into CFSR using a 3D variational data assimilation (3DVAR) scheme. Temperature of the top layer (SST) is strongly nudged to the daily Optimum Interpolation SST (OISST) product–based AVHRR and AMSR satellite measurements and in situ data from ships and buoys (Reynolds et al. 2007). For a detailed description of the CFSR's features, readers are referred to Saha et al. (2010) and Xue et al. (2011). According to assessments of Xue et al. (2011) and Wang et al. (2011), CFSR can much better represent the mean structure and variability of the tropical atmosphere and ocean than its early versions. In particular, tropical intraseasonal precipitation is greatly improved (Wang et al. 2012).

c. OGCM experiments

The Hybrid Coordinate Ocean Model (HYCOM) version 2.2.18 (Halliwell 2004; Wallcraft et al. 2009) is utilized to understand the ocean processes governing intraseasonal SST variability. HYCOM is configured to the Indian Ocean basin within 50°S–30°N, 30°–122.5°E with a horizontal resolution of 0.25° × 0.25° and 26 hybrid vertical layers (Li et al. 2014, 2015). The layer thickness gradually enlarges from ~2.6 m near the surface to ~500 m in the deep ocean. At the western, eastern, and southern open-ocean boundaries 5° sponge layers are applied, in which the model temperature and salinity are relaxed to the *World Ocean Atlas* (*WOA*) climatology. The surface forcing fields of HYCOM include 0.75° × 0.75° 2-m air temperature and humidity from the European Centre for Medium-Range Weather Forecasts (ECMWF) interim reanalysis (ERA-Interim) products (Dee et al. 2011), surface net SWR and LWR from the CERES product, precipitation from TMPA level 3B42 V7 product, and surface wind speed and wind stress calculated from CCMP 10-m winds. Note that in our model, wind speed and wind stress are separately imposed on the model ocean. While wind stress affects SST via ocean dynamical and mixed layer processes (e.g., horizontal advection, upwelling, and turbulent mixing), wind speed affects SST through turbulent heat flux (latent heat flux plus sensible heat flux). In our model, turbulent heat flux is calculated from surface wind speed, air temperature, specific humidity, and model (instead of observed) SST using the Coupled Ocean–Atmosphere Response Experiment (COARE 3.0) algorithm (Kara et al. 2005) and consequently includes feedback from SST variability. Monthly river discharge records of Papa et al. (2010) and Dai et al. (2009) are used as lateral freshwater flux forcing.

The model is spun up from a state of rest for 30 years under monthly climatologic atmospheric forcing of the 2000–11 period. Restarting from the already spun up solution, HYCOM is integrated forward from March 2000 to November 2011, a period determined by the availability of CERES radiation and CCMP winds at the time when the model experiments were performed. The main run (MR) is forced with the original daily forcing. Its solution contains the complete processes and is compared

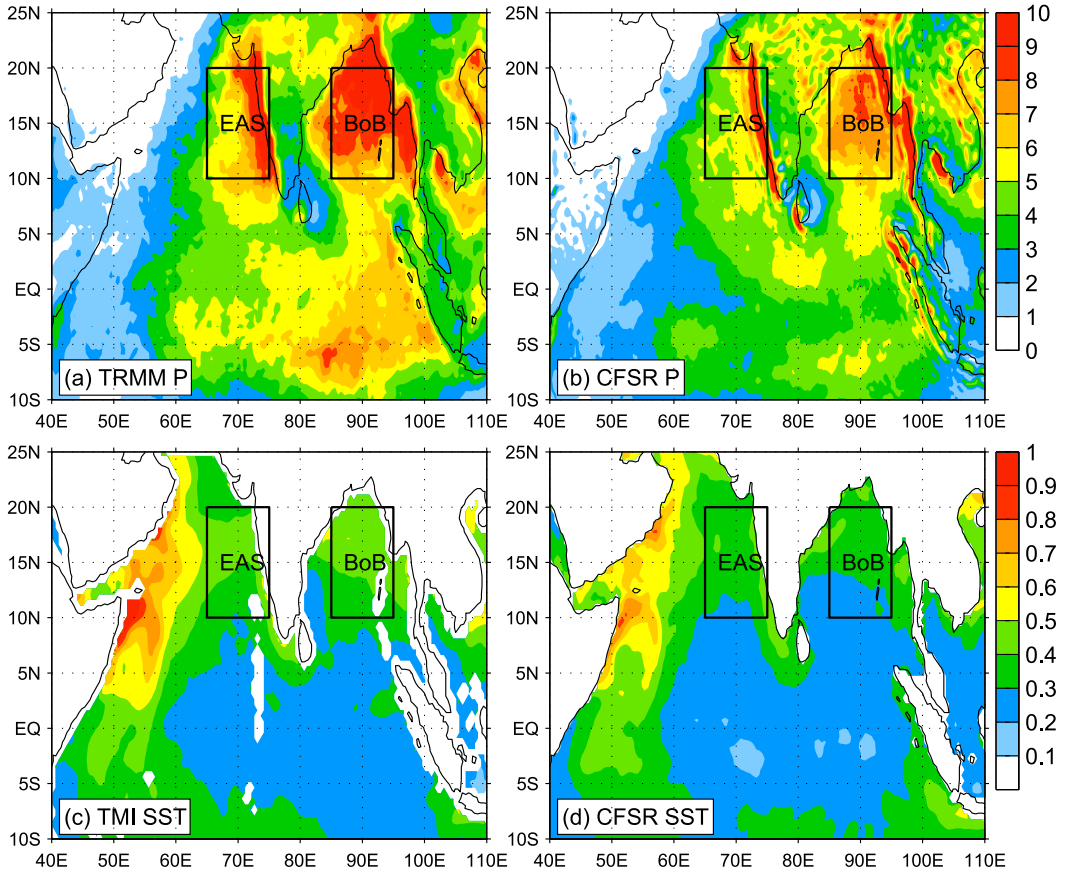

FIG. 2. STD of 20–90-day precipitation (mm day^{-1}) for the ISM season (15 May–15 October) based on (a) TRMM and (b) CFSR products of 1998–2010. STD of 20–90-day SST (°C) for the ISM season based on (c) TMI and (d) CFSR products of 1998–2010. The black rectangles define the areas of the EAS (10°–20°N, 65°–75°E) and the BoB (10°–20°N, 85°–95°E).

with observations to evaluate model performance. The MISOs induce intraseasonal SST variability mainly through three effects: SWR, wind speed–controlled turbulent heat fluxes, and wind stress–driven oceanic processes (advection, upwelling, and mixing). Here the three effects on SST are isolated via three parallel HYCOM experiments. In the NoSWR experiment, the daily SWR is filtered with a 105-day low-pass Lanczos digital filter, and the other forcing fields are the same as in MR. The intraseasonal (20–90 day) SST in the difference, MR − NoSWR, can therefore measure the SWR effect of MISOs on SST. In NoWND both wind speed and wind stress are 105-day low-pass filtered, while in the NoTAU experiment only wind stress is low-pass filtered. Therefore, the difference MR − NoTAU quantifies the wind stress forcing effect of MISOs on SST, while the NoTAU − NoWND solution measures the wind speed effect on SST through turbulent heat flux. Results of the four experiments are stored in 3-day mean resolution. To exclude the transient effect from the spinup run, we ignore the output of year 2000, and the 11-yr data of 2001–11 are used for analysis.

3. Variability of SST and precipitation associated with the MISOs

a. Observations and CFSR

In this study the ISM season is broadly defined as the period of 15 May–15 October, and the standard deviation (STD) of 20–90-day precipitation during ISM season represents the intensity of intraseasonal precipitation variability associated with MISOs (Fig. 2a). The distribution of precipitation STD generally resembles the mean precipitation pattern in Fig. 1, with two variance maxima located in the EAS and BoB where the mean precipitation is large. In the EAS, large variations with STD > 9 mm day^{-1} occur near the western coast of India. Over the BoB, large intraseasonal variations with STDs > 8 mm day^{-1} cover both the coastal region and interior bay. The two variance maxima are accompanied

by weaker variations near the equator, indicating that the MISOs strengthen as they propagate northward from the equator. Strong variations with STDs of 6–8 mm day^{-1} are seen to the south of the equator in the central-to-eastern Indian Ocean basin, corresponding to the intertropical convergence zone (ITCZ), along which the Madden–Julian oscillations propagate eastward. Intraseasonal variability of precipitation in CFSR product (Fig. 2b) has an overall agreement with TRMM data. Yet strong variations in CFSR are more confined to the eastern boundary areas of the EAS and BoB, with much weaker variations in the basin interior. Similar to precipitation, SST also shows prominent intraseasonal variability in the BoB and Arabian Sea (Fig. 2c). The strongest SST signals, however, appear along the Somalia–Oman coast in the western Arabian Sea, with a STD exceeding 0.6°C. These SST variations arise primarily from ocean internal instabilities of the western boundary currents and are generally not related to the MISOs (Jochum and Murtugudde 2005; Duncan and Han 2009; Vialard et al. 2012). Instead, SST variations in the EAS and BoB, with an STD of 0.3°–0.5°C, are primarily induced by MISOs and possibly involved in the MISO dynamics (Kemball-Cook and Wang 2001; Roxy and Tanimoto 2007; Duncan and Han 2009; Vialard et al. 2012). To capture the prominent rainfall and SST signatures of MISOs in the two regions, we define the EAS box (10°–20°N, 65°–75°E) and the BoB box (10°–20°N, 85°–95°E). Similar to precipitation, SST variability in CFSR (Fig. 2b) exhibits realistic spatial distribution, while its amplitude is smaller than TMI observation by up to 0.1°C.

Daily precipitation time series averaged over the EAS and BoB boxes exhibit pronounced intraseasonal variability during the ISM season (Fig. 3). A close inspection reveals a striking difference between the two regions. In the EAS, precipitation tends to have stronger fluctuations at the beginning of the ISM season (Fig. 3a), showing more strong convection events in May and June. This feature is identifiable in almost every year, particularly in 1999, 2001, 2002, 2003, 2005, 2006, 2007, 2008, 2010, and 2013. This feature, however, is absent in the BoB, although the total ISM rainfall is larger than that of the EAS (Fig. 3b). For convenience, hereafter we divide the ISM period into three stages: the developing stage of 15 May–31 June, the mature stage of 1 July–31 August, and the decaying stage of 1 September–15 October. Figures 3c–e compare the STD maps of 20–90-day precipitation of the three stages. Along the west coast of India the precipitation variability is even slightly stronger in the mature stage than in the developing stage, but in the interior Arabian Sea basin precipitation variability is much stronger in the developing stage. Such spatial pattern implies that ocean processes may play a role in the enhanced MISO intensity in the developing stage of the ISM, which requires in-depth investigation.

To reveal the common characteristics of MISOs, we conduct a composite analysis, a method widely used in MISO research (e.g., Jiang et al. 2004; Wang et al. 2009; Sharmila et al. 2013). The MISO convective events are identified as the maxima of 20–90-day precipitation exceeding one STD value (Fig. 4a). Under this criterion, 48 MISO events occurred in the EAS during 1998–2010. The MISO events from CFSR are quite consistent with those from TRMM data, showing 44 events for the same period (Fig. 4b). These events are utilized for the composite. Specifically, the precipitation peak is taken as the zero day, and then 20–90-day bandpass-filtered ocean and atmospheric variables from these events are averaged for each day from −30 day to +30 day. Figure 5a shows the composites of TRMM precipitation and TMI SST between 65° and 75°E (longitude range of the EAS box) based on the 48 events. The positive precipitation anomaly, representing the convection center, can be traced back to the equator on −10 day and moves to 20°N on +7 day, indicating a mean propagation speed of ~1.5 m s^{-1} (1.18° latitude day^{-1}). Precipitation and SST exhibit a clear quadrature phase relationship, with a warm SST anomaly of 0.4°–0.5°C leading precipitation event, which is followed by a cold SST anomaly of 0.3°–0.4°C. These characteristics are approximately consistent with the earlier results attained by Roxy and Tanimoto (2007) and Roxy et al. (2013). The CFSR composites generally produce realistic large-scale precipitation structures and the quadrature phase relationship between precipitation and SST (Fig. 5b), but its SST signals are much weaker. The SST maxima of CFSR are located near the northern boundary (~20°N) rather than at the latitude of the precipitation maximum (15°–16°N) as in observation.

The relationship between intraseasonal SST and precipitation is an important aspect of the MISO characteristics and provides indications for air–sea interaction (e.g., Goswami 2005; Roxy et al. 2013; Xi et al. 2015). Temporal evolutions of the EAS-averaged SST and precipitation of the composite MISO are plotted in Fig. 5c. Positive SST anomaly, with a composite magnitude of ~0.4°C, occurs 5–6 days before the precipitation event (black curve in Fig. 5c). This response time of convection to warm SST is much shorter than in the BoB and South China Sea (~12 days; Roxy et al. 2013). Roxy et al. (2013) demonstrated that the strong surface background wind convergence, established by the zonal SST gradient in the Arabian Sea, accelerates the upward motion of anomalous moist air and leads to a quicker response of regional precipitation to SST anomaly. The

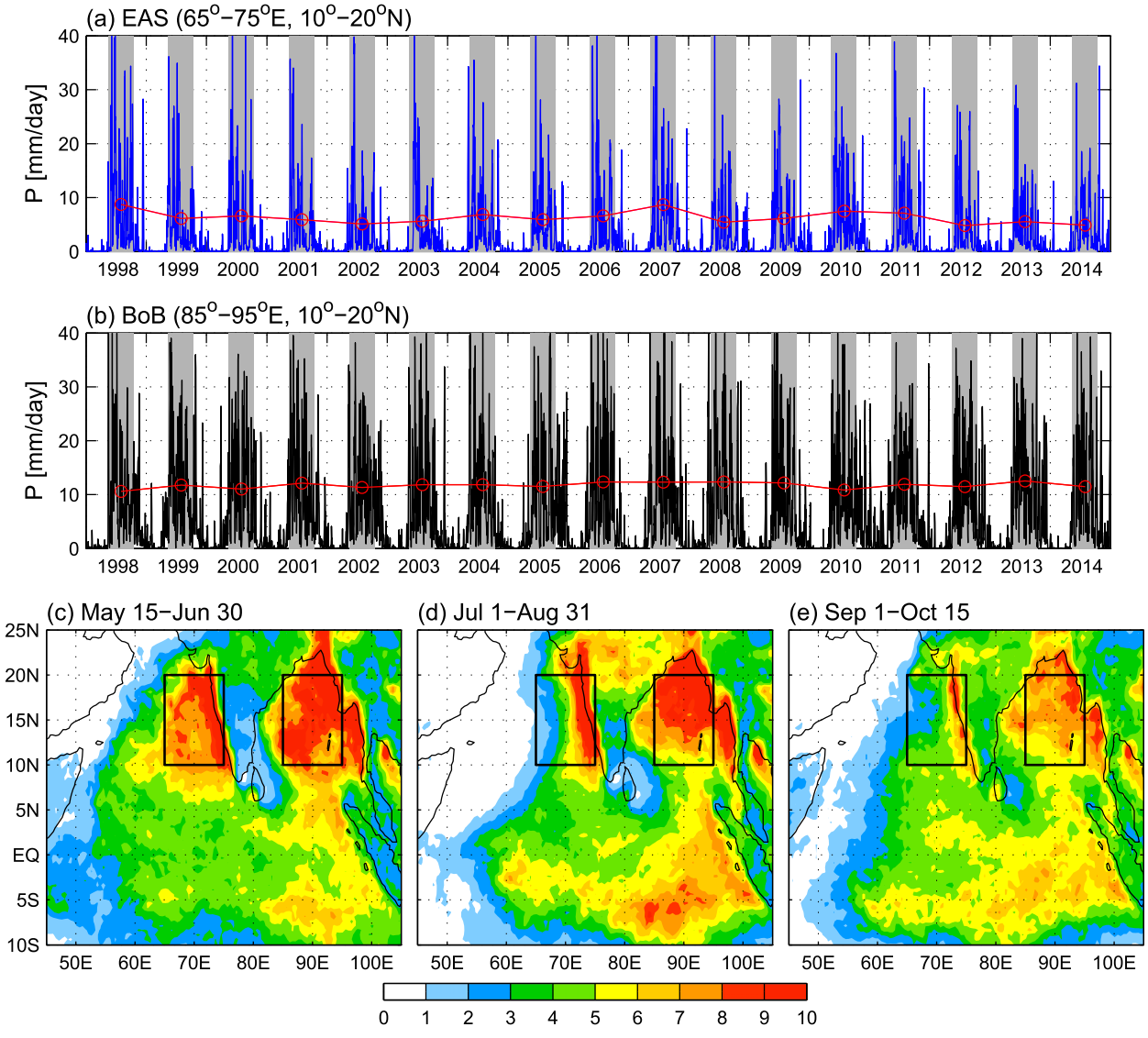

FIG. 3. Daily TRMM precipitation averaged over (a) the EAS and (b) the BoB. Gray shadings denote the ISM season of 15 May–15 October. The red lines with circles denotes the ISM-mean precipitation for each year. STD maps of 20–90-day TRMM precipitation (mm day^{-1}) for the (c) developing stage (15 May–30 June), (d) mature stage (1 July–31 August), and (e) decaying stage (1 September–15 October) of the ISM.

convection of the MISO is accompanied with reduced net surface heat flux Q_{net} (blue curve; the sum of SWR, LWR, and Q_T), which is the major cause for the postevent SST decrease. The SST minimum in the composite occurs around +9–+10 day, indicating a 9–10-day response time of SST to atmospheric forcing. The CFSR can faithfully represent the changes in precipitation and Q_{net} (Fig. 5d), but its SST anomaly is only ~0.2°C, accounting for only half of the observed magnitude. In CFSR the precipitation occurs 8–9 days after the warm SST, which is later than in observations by ~3 days. On the other hand, the postevent cold SST occurs on +7 day, indicating a quicker response of SST in CFSR to MISO forcing than in observations. Apparently, CFSR has underestimated intraseasonal SST variability in the EAS. As a result, the large impact of SST on MISO convection, as reflected by the quick response of atmospheric convection to SST anomaly, is probably also underrepresented. As the major cause of SST anomaly, Q_{net} anomaly is contributed by both SWR and turbulent heat flux Q_T. The partitioning between the two components, however, shows divergence between observational estimates and CFSR product. CFSR has smaller SWR anomaly than CERES data and larger Q_T anomaly than OAFlux. These discrepancies may also contribute to the errors of SST in CFSR.

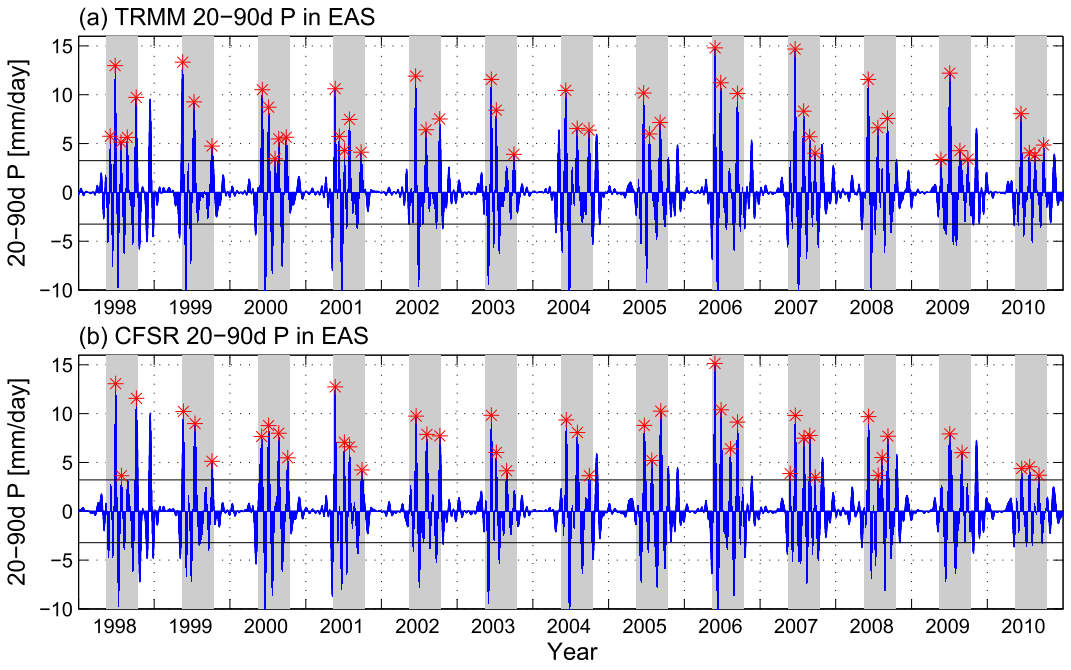

FIG. 4. (a) The 20–90-day TRMM precipitation averaged over the EAS box used for the selection of MISO events. Gray shadings denote the ISM season. Red asterisks mark the precipitation maxima exceeding one STD value (black horizontal lines), which are used to identify intraseasonal convection events. (b) As in (a), but based on CFSR data.

Despite a strong nudging toward the satellite-based daily OISST (section 2b), CFSR SST represents the bulk SST of the top 10 m, whereas TMI satellite SST measures skin temperature. In fact, the OISST employs an adjustment of satellite measurements with respect to in situ data (Reynolds et al. 2007) and hence also to a large extent represents the bulk temperature. A composite analysis of the OISST shows that its intraseasonal variability is also weaker than TMI SST by 20% but still stronger than CFSR (figures not shown).

The underestimation of intraseasonal SST in the first-guess value of CFSR could—at least partly—result from the bulk effect, indicating the importance of simulating/parameterizing the diurnal skin layer in CFSv2 to improve the MISO and ISM prediction.

b. *MISO intensity variation*

As shown in Fig. 3, MISOs in the EAS tend to be stronger in the developing stage of the ISM. As suggested by many studies, the MISO intensity is sensitive to the background conditions of the ocean and atmosphere (e.g., Qi et al. 2008; Roxy et al. 2013; Sabeerali et al. 2014). With the evolution of monsoon winds (Fig. 1), the ocean background state undergoes prominent variation during the ISM season. Figure 6 shows the monthly climatologic SST and MLD from satellite and in situ observations. Here MLD is computed in the same method as in CFSR product, adopting a criterion of density increase of 0.25 kg m^{-3} from the surface to mixed layer bottom (Xue et al. 2011). The Arabian Sea has a striking high SST (>30°C) and shallow MLD (~30 m) in May, owing to the weak winds and reduced Q_T during the monsoon transition period (Murtugudde et al. 2007). With the development of the ISM, the southwesterly monsoon winds cool the SST and deepen the MLD via downwelling, increased Q_T, and enhanced turbulent mixing (de Boyer Montégut et al. 2007; Murtugudde et al. 2007; Izumo et al. 2008). In the mature stage of the ISM (July–August), SST in the Arabian Sea interior is decreased to <28°C and MLD is deepened to 50–90 m. As the ISM decays in September–October, the shallow MLD and warm SST are reestablished. Averaged over the EAS box, the shallow–deep–shallow evolution of MLD and high–low–high change in SST throughout the ISM period are clearly displayed and also faithfully reproduced by CFSR (Fig. 7a). During the ISM developing stage, however, CFSR produces a ~5-m thicker MLD than the observed (Fig. 7a). Year-to-year variation of MLD for each month, as indicated by the vertical bars in Fig. 7a, is much weaker than its seasonal variation, further assuring the robustness of the seasonal change. In comparison, variations in the BoB region are less prominent (Fig. 7b), corresponding to the smaller change in winds (Fig. 7d).

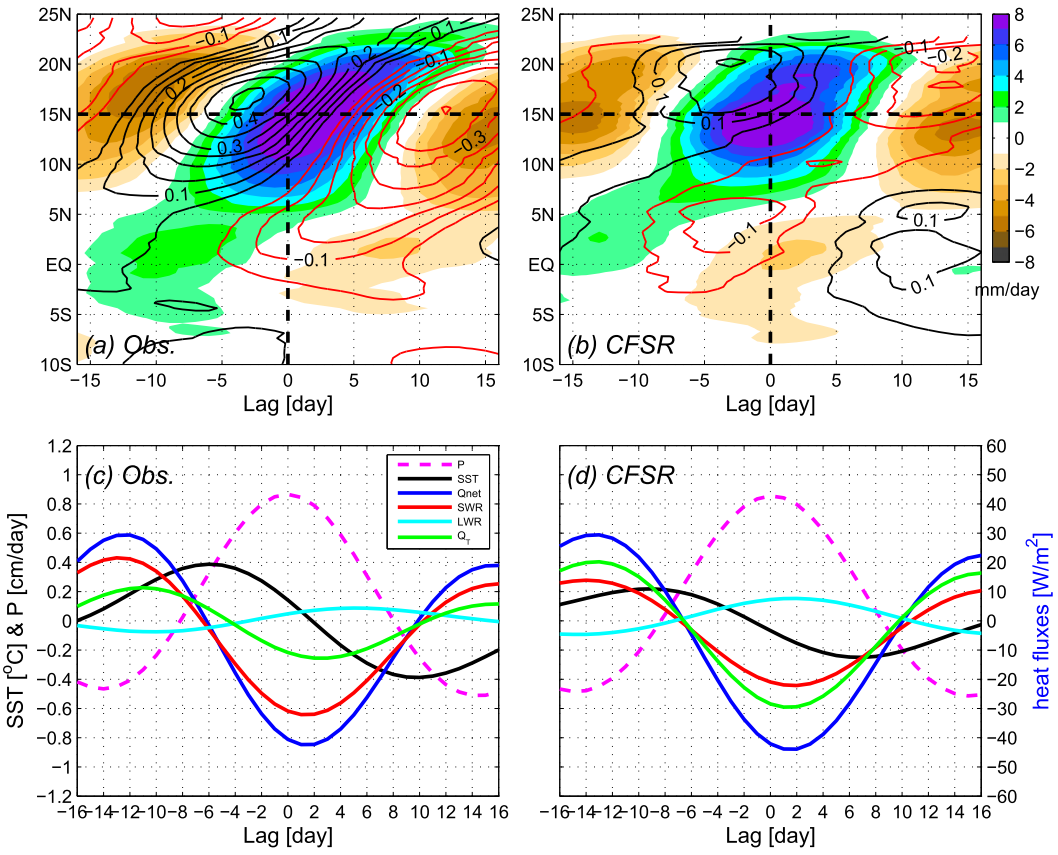

FIG. 5. (a) Time–latitude plot of the composite MISO precipitation (color shading; mm day^{-1}) and SST (black contours for positive and red contours for negative; °C) averaged between 65° and 75°E from TRMM and TMI data; (b) as in (a), but for CFSR data. (c) Precipitation (dashed purple; cm day^{-1}), SST (black; °C), surface net heat flux Q_{net} (blue; W m^{-2}), SWR (red), LWR (cyan), and turbulent heat flux Q_T (green) of the composite MISO event averaged over the EAS box from observational datasets; (d) as in (c), but for CFSR data. The 20–90-day filtered data are used for computing the composites, and the precipitation maximum is taken as day zero of the composite.

While MLD affects SST response to MISOs (e.g., Roxy et al. 2013; Li et al. 2014), background SST magnitude influences the response of atmospheric convection to SST anomaly (e.g., Gadgil et al. 1984; Graham and Barnett 1987; Waliser et al. 1993). Therefore, the shallow MLD and high SST in the Arabian Sea in the developing stage may favor intraseasonal air–sea interaction and therefore contribute to the observed enhancement of MISOs (Fig. 3). To confirm the variation in MISO intensity, we perform the composites separately for each ISM stage, using the 18, 16, and 14 events that occurred in the developing, mature, and decaying stages, respectively. The composite MISO in the developing stage is indeed the strongest in both precipitation and SST among the three (Fig. 8a), followed by the decaying stage composite, which has stronger anomalies south of 14°N. The mature stage composite is overall the weakest, considering both precipitation and SST. It is interesting to note that compared to the mature stage, the precipitation signals in the decaying stage are weaker at some latitudes, whereas its SST anomalies are significantly larger. This phenomenon provides a clear indication for the effect of MLD, given that the shallow MLD in the decaying stage can amplify the SST response to atmospheric forcing. Similar composite analysis is also conducted for the BoB region (Fig. 8b). For precipitation, the difference in the three stages is not evident, with the developing stage slightly weaker than the other two. SST variations are larger in the decaying stage owing to both stronger atmospheric forcing and perhaps also a shallower MLD. Compared to the BoB, the EAS has much stronger seasonal variations of SST and MLD, which are likely causing the observed MISO intensity variation via modulating intraseasonal SST and air–sea interaction. This effect will be further explored in section 4. The seasonal variation of MISO intensity in the EAS is also reproduced by CFSR (Fig. 8c). In particular, the enhancements of precipitation signals in the developing stage and SST signals in the decaying stage are even more evident than in observations.

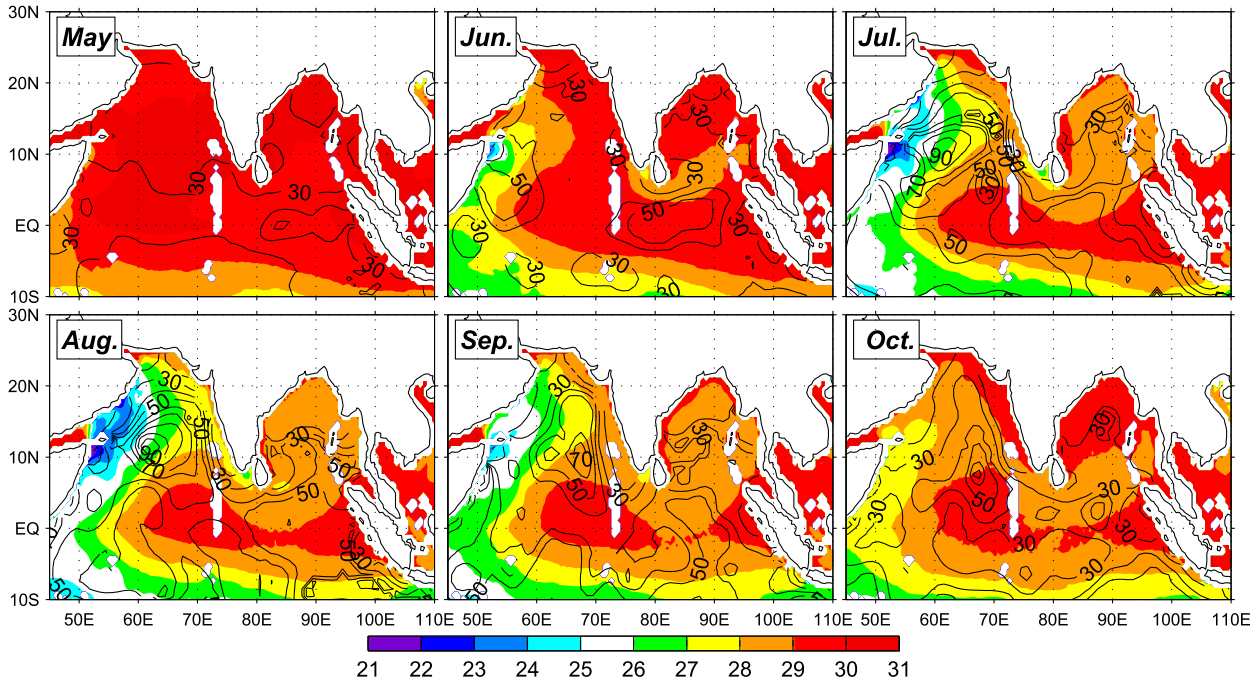

FIG. 6. Monthly climatology of SST (color shading; °C) from TMI data and MLD (black contours; m) based on gridded Argo data (Hosoda et al. 2008) for 2001–11.

4. Processes

a. Causes for intraseasonal SST variability

To achieve an in-depth understanding of the MLD impact, we need to clarify the processes controlling intraseasonal SST variability in the EAS region. Effects of these processes can be isolated and evaluated through HYCOM experiments (section 2c). Before that, we need to verify the performance of HYCOM. HYCOM MR produces a realistic distribution of intraseasonal SST variability during the ISM season (Fig. 9a), resembling that based on satellite measurements (Fig. 2c). In the EAS region, the modeled 20–90-day SST agrees with TMI data (Fig. 9b), achieving a linear correlation of 0.87 (significant at the 99% confidence level) during 2001–11. The amplitude of intraseasonal SST is weaker than observation by ~17%, with an STD of 0.29° versus 0.35°C for TMI data. This discrepancy may result largely from the fact that HYCOM SST is the bulk temperature of the top 2.6-m layer, which has weaker variability than the skin temperature measured by the satellite. In addition, with daily SWR forcing, our HYCOM simulation does not resolve the diurnal cycle of ocean temperature, which can enhance the intraseasonal SST amplitude by 10%–20% in the tropical Indian Ocean (e.g., Bernie et al. 2007; Y. Li et al. 2013). HYCOM has also well reproduced the seasonal variations of SST and MLD during the ISM (Fig. 9c). The simulated MLD compares even more favorably with Argo observations than CFSR. In addition, HYCOM has well simulated the SST anomalies of the MISO composite in the three stages of the ISM (Fig. 10). The magnitude, spatiotemporal structure, and strength variation of the composite SST anomalies from HYCOM are all consistent with observations. Therefore, HYCOM is successful in simulating the upper-ocean variability of the EAS region, lending us the confidence for further investigation of the underlying processes using the HYCOM experiments.

Existing studies suggest that MISOs can induce SST variability in the tropical Indian Ocean primarily through three effects (e.g., Waliser et al. 2004; Duncan and Han 2009; Vialard et al. 2012): the SWR effect, wind speed–controlled Q_T (or wind speed effect), and wind stress–driven oceanic processes (wind stress effect). The three effects are measured, respectively, by solution differences of MR − NoSWR, NoTAU − NoWND, and MR − NoTAU (section 2c). As shown by the MISO composite in the EAS, SST anomalies induced by the three effects are comparable (Fig. 11a). Their contributions to the pre-event SST warming are roughly equal, while the wind speed effect makes a larger contribution to the postevent cooling than the other two. The sum of the three effects (gray) is close to the total SST, indicating that the nonlinear interaction between different effects is generally small.

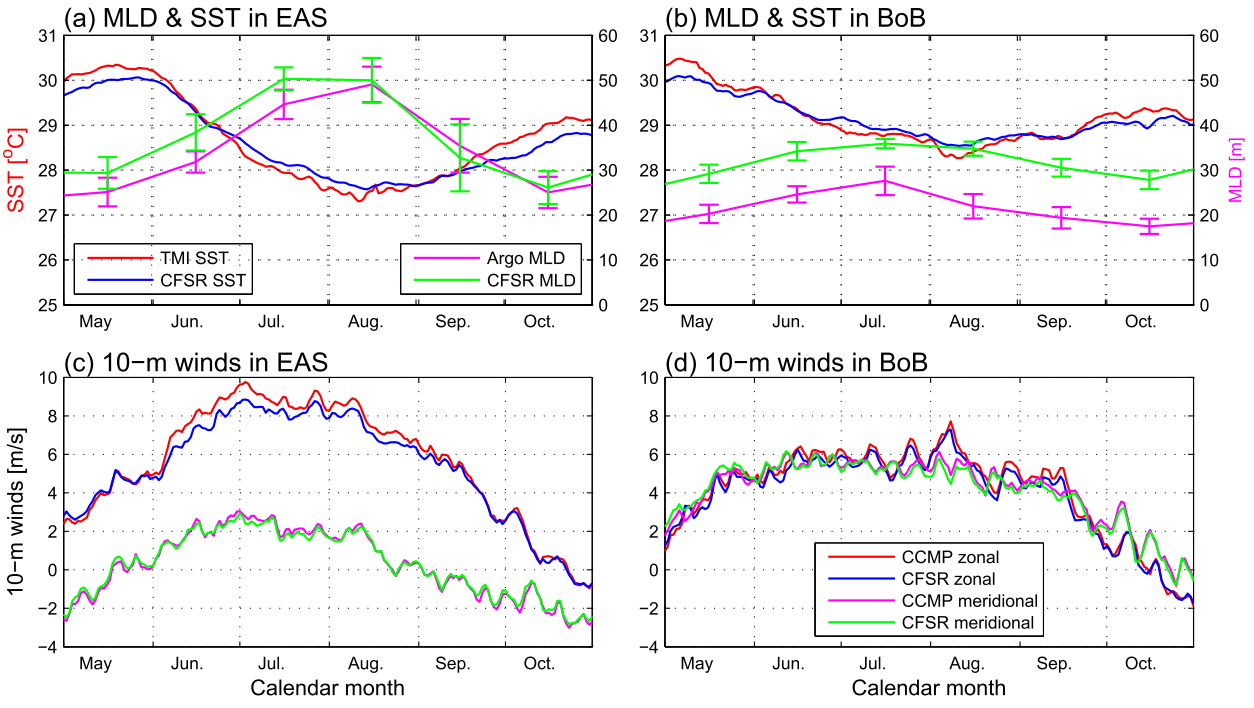

FIG. 7. (a) Climatologic monthly MLD and climatologic daily SST averaged over the EAS box based on gridded Argo data, TMI data, and CFSR for 1998–2010; (b) as in (a), but for the BoB box. The vertical bars on MLD denote its STD range for each month, measuring the year-to-year variability. (c) Climatologic daily CCMP 10-m winds averaged for the EAS and CFSR for 1998–2010; (d) as in (c), but for the BoB box.

To further identify the processes responsible for intraseasonal SST variability, a mixed layer heat budget analysis is performed for the EAS region using MR results. The temporal tendency of mixed layer temperature $[T]$ is determined by surface heat flux forcing SHF, horizontal advection ADV, and vertical entrainment ENT:

$$\partial[T]/\partial t = \mathrm{SHF} + \mathrm{ADV} + \mathrm{ENT} + R. \quad (1)$$

In the above, the square brackets denote the mean value of the surface mixed layer, and the SHF is determined by the total heat flux absorbed by the mixed layer Q and MLD H:

$$\mathrm{SHF} = \frac{Q}{c_p \rho_0 H}, \quad (2)$$

where Q is computed as the difference between surface net heat flux Q_{net} and the penetrating SWR at the bottom of the mixed layer Q_{pen}; that is, $Q = Q_{\mathrm{net}} - Q_{\mathrm{pen}}$, and c_p and ρ_0 are the specific heat capacity and density of seawater averaged over the mixed layer of the EAS. Here, Q_{pen} is computed as with the formula of Halliwell (2004):

$$Q_{\mathrm{pen}} = \mathrm{SWR} \times \left[r \exp\left(\frac{-H}{\beta_R}\right) + (1-r) \exp\left(\frac{-H}{\beta_B}\right) \right], \quad (3)$$

where $r = 0.62\%$ is the red light fraction, $\beta_R = 0.60$ is the penetration depth scale of red light, and $\beta_B = 20.0$ is the penetration depth scale of blue light for the Jerlov water type IA adopted in our model configuration. ADV is calculated as follows:

$$\mathrm{ADV} = -[\mathbf{u} \cdot \nabla T], \quad (4)$$

where $\mathbf{u} = (u, v)$ is the horizontal current vector, and $\nabla T = (\partial T/\partial x, \partial T/\partial y)$ is the horizontal temperature gradient. Following Stevenson and Niiler (1983), ENT is calculated as follows:

$$\mathrm{ENT} = -\frac{[T] - T_{-H}}{H} \times \left(w_{-H} + \frac{\partial H}{\partial t} + \mathbf{u}_{-H} \cdot \nabla H \right), \quad (5)$$

where T_{-H} and w_{-H} are the temperature and vertical velocity at the mixed layer bottom, $\partial H/\partial t$ is the local MLD tendency, and $\mathbf{u}_{-H} \cdot \nabla H$ is the MLD change induced by horizontal advection. Note that the effect of upwelling is also included in ENT, reflected in the values of w_{-H} and T_{-H}. The term R is the residual term, representing the unresolved processes such as diffusion and errors in the estimation of other terms. The MISO composite of the heat budget terms is shown in Fig. 11b. Note that the mean values of these terms are retained in order to denote their overall warming or cooling effects on SST. Throughout the composite MISO event, SST anomaly is predominantly induced by SHF, confirming the important contributions of SWR and Q_T. ENT is

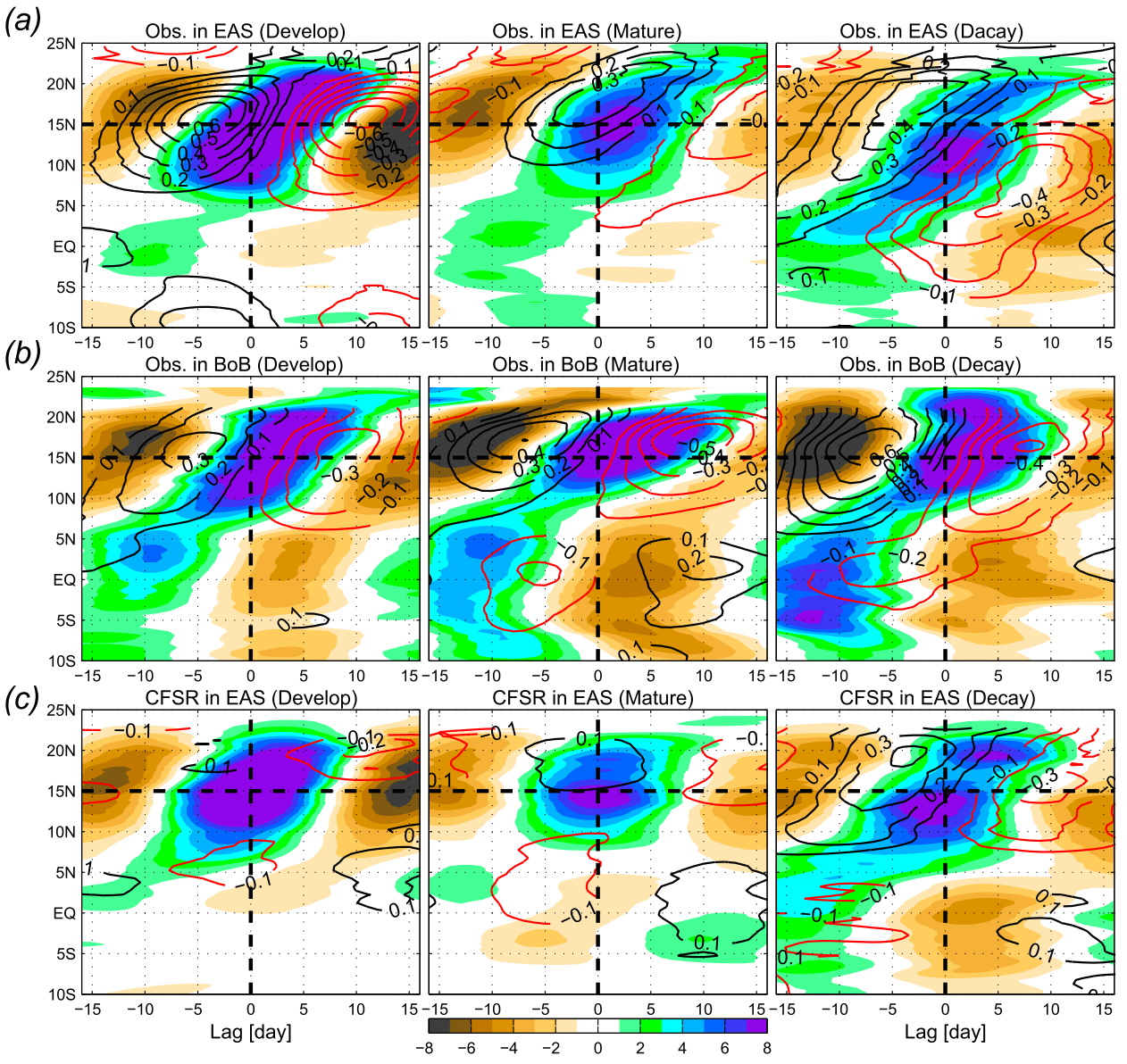

FIG. 8. (a) Evolutions of TRMM precipitation (color shading; mm day^{-1}) and TMI SST (contours; °C) of the composite MISO in the longitude band of the EAS (65°–75°E) for the (left) developing stage, (center) mature stage, and (right) decaying stage of the ISM; (b) as in (a), but for the MISO composite in the BoB band (85°–95°E); (c) as in (a), but for CFSR precipitation and SST.

relatively small in magnitude, but it contributes ~10% to the SST cooling during the convection peak. ADV is also small and is generally out of phase with $\partial[T]/\partial t$. The residual term R shows a mean value of -0.015°C day^{-1}. It may arise from the overestimation of the SHF warming effect or represent the effect of ignored processes, such as diffusion. Note that the variation of R is out of phase with $\partial[T]/\partial t$. It means that the primary forcing processes for SST have already been captured by the heat budget analysis.

Among the three terms, ADV and ENT are controlled mainly by wind stress, while SHF is controlled by Q that is contributed by SWR and Q_T (LWR is unimportant as shown in Fig. 5) and MLD that is primarily determined by winds stress in HYCOM. To better understand the wind stress effect on SST, we further compare the MR (with wind stress effect) and NoTAU (without wind stress effect) experiments. Variation of $\partial[T]/\partial t$ from NoTAU is weaker than that of MR in both the pre-event warming and postevent cooling (Fig. 11c). The total amplitude is smaller by ~0.02°C day^{-1}, which is roughly consistent with the ~30% contribution of wind stress effect in Fig. 11a. Wind stress has a large effect on SHF term, especially

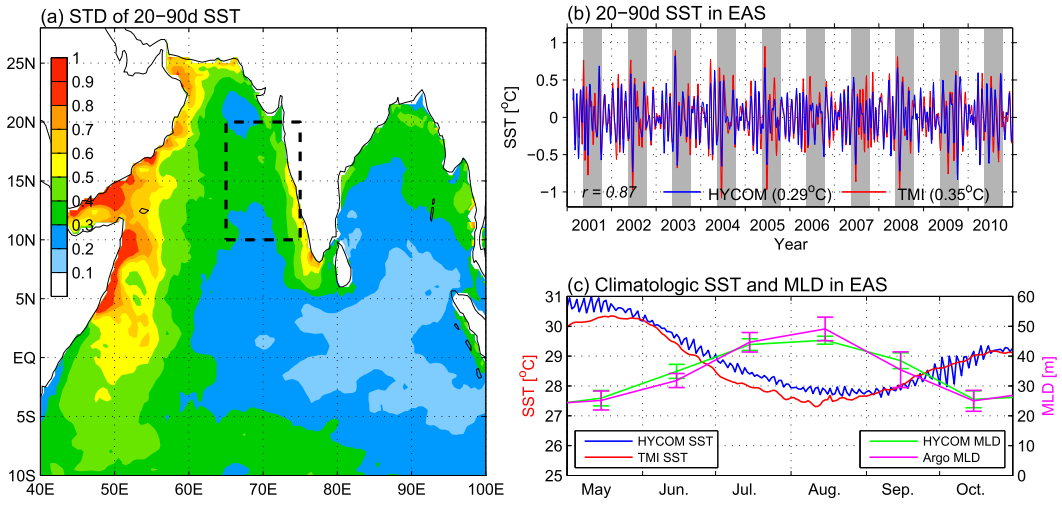

FIG. 9. HYCOM MR results during 2001–11: (a) STD of 20–90-day SST (°C) for the ISM season; (b) 20–90-day SST averaged over the EAS (blue) compared to TMI SST (red); and (c) climatologic daily SST (blue) and monthly MLD (green) averaged over the EAS compared to TMI SST (red) and Argo MLD (purple). In (c), the vertical bars on MLD denote its STD range for each month, measuring the year-to-year variability.

the pre-event warming (Fig. 11d). Figure 11e compares the total heat flux Q, which shows little difference between MR and NoTAU. In the precondition phase Q is in fact slightly smaller in MR than in NoTAU. Therefore, the larger SHF in MR is due to the shallower MLD (figure not shown), which increases the mixed layer warming rate during the precondition phase. On the other hand, Fig. 11f shows that wind stress is the primary driver of ENT, which contributes to SST variability by about 0.01°C day^{-1}. These results suggest that through changing MLD, the MISO's wind stress is involved in two processes associated with SST variability: heat flux forcing at the sea surface and entrainment at the base of the mixed layer, although the effect of the latter is much smaller.

b. *Impact of MLD*

The analysis in section 4a demonstrates that the most important process for SST variability in the EAS is surface heat flux forcing. According to Eq. (2), the magnitude of SHF is sensitive to changes of the background MLD. A shallow background MLD can amplify the SHF magnitude. To quantify such impact, we recalculate the SHF term using the ISM seasonal mean MLD H_m in order to remove the impact of MLD change in SHF:

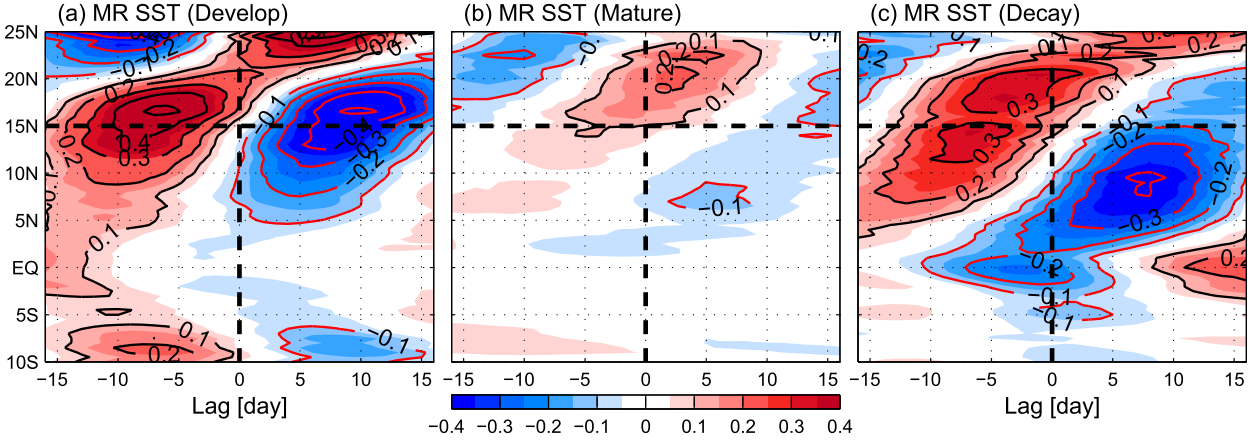

FIG. 10. SST (°C) of the composite MISO in the longitude band of the EAS (65°–75°E) for the (a) developing stage, (b) mature stage, and (c) decaying stage of the ISM based on HYCOM MR output.

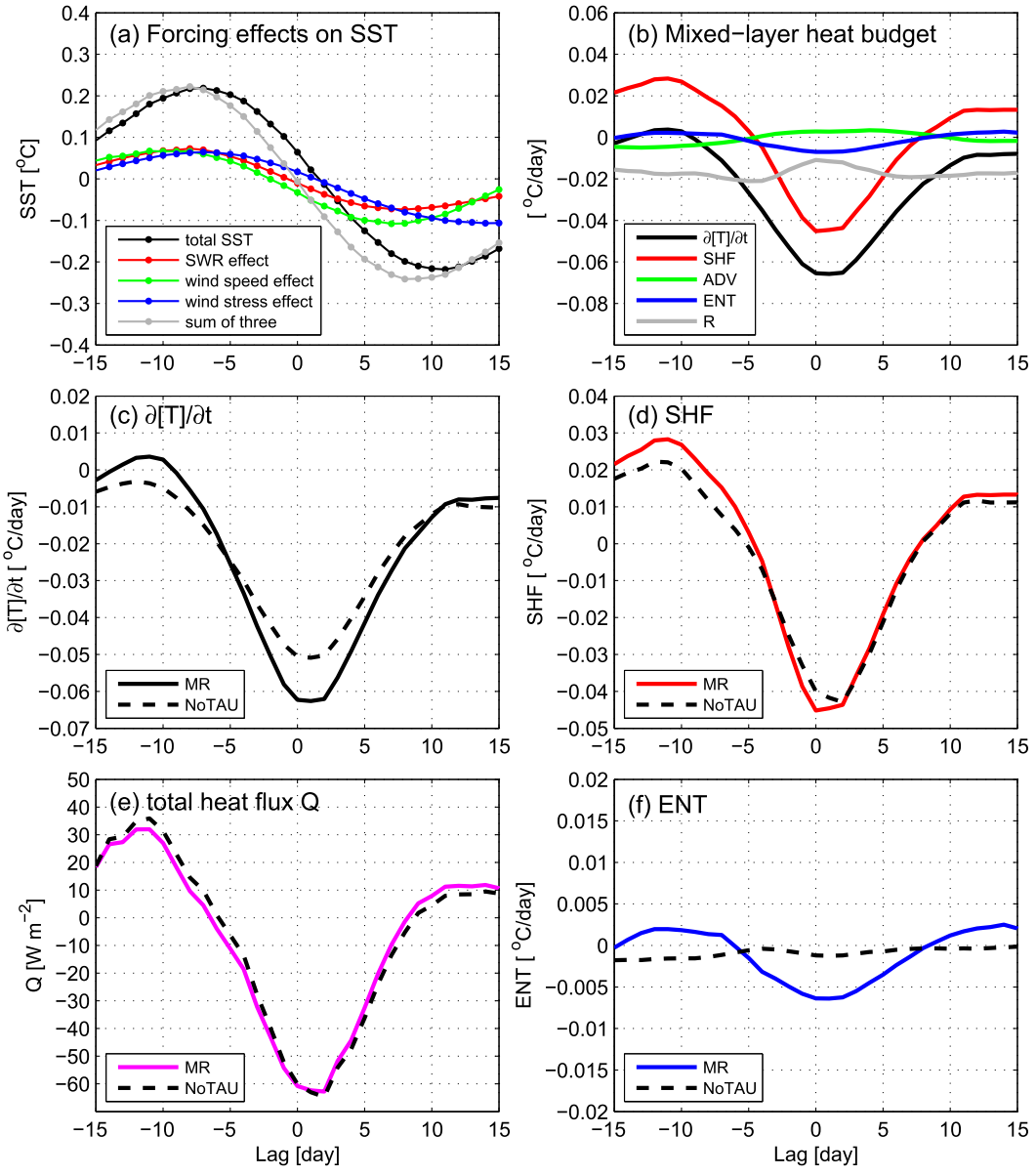

FIG. 11. (a) The 20–90-day SST of the composite MISO averaged over the EAS from HYCOM MR (black) and those produced by SWR effect (red; from MR − NoSWR), wind speed effect (green; from NoTAU − NoWND), wind stress effect (blue; from MR − NoTAU), and the sum of the three effects (gray). (b) Mixed layer heat budget of the composite MISO for the EAS: mixed layer temperature tendency $\partial[T]/\partial t$ (black solid), surface heat flux forcing term SHF (red), horizontal advection term ADV (green), vertical entrainment term ENT (blue), and the residual term R (gray) computed from MR output; (c) $\partial[T]/\partial t$, (d) SHF, (e) total heat flux Q, and (f) ENT terms computed from MR output (solid) and NoTAU output (black dashed).

$$\mathrm{SHF}_m = \frac{Q}{c_p \rho_0 H_m}. \tag{6}$$

The difference between SHF and SHF_m measures the effect of MLD change. Figure 12 compares the total SHF and SHF_m values for the MISO composites in the three stages. In the developing stage, results from HYCOM MR show that the variation of SHF is visibly larger than SHF_m (Fig. 12a). The shallow MLD nearly doubles the precondition warming and enlarges the postevent cooling by ~20%. In the mature stage, the MLD effect is rather small (Fig. 12b), possibly owing to the small SHF magnitude. In the decaying stage, SHF has a warming effect throughout the MISO event (Fig. 12c). The shallow MLD increases the warming rate and significantly amplifies the SHF variation with a

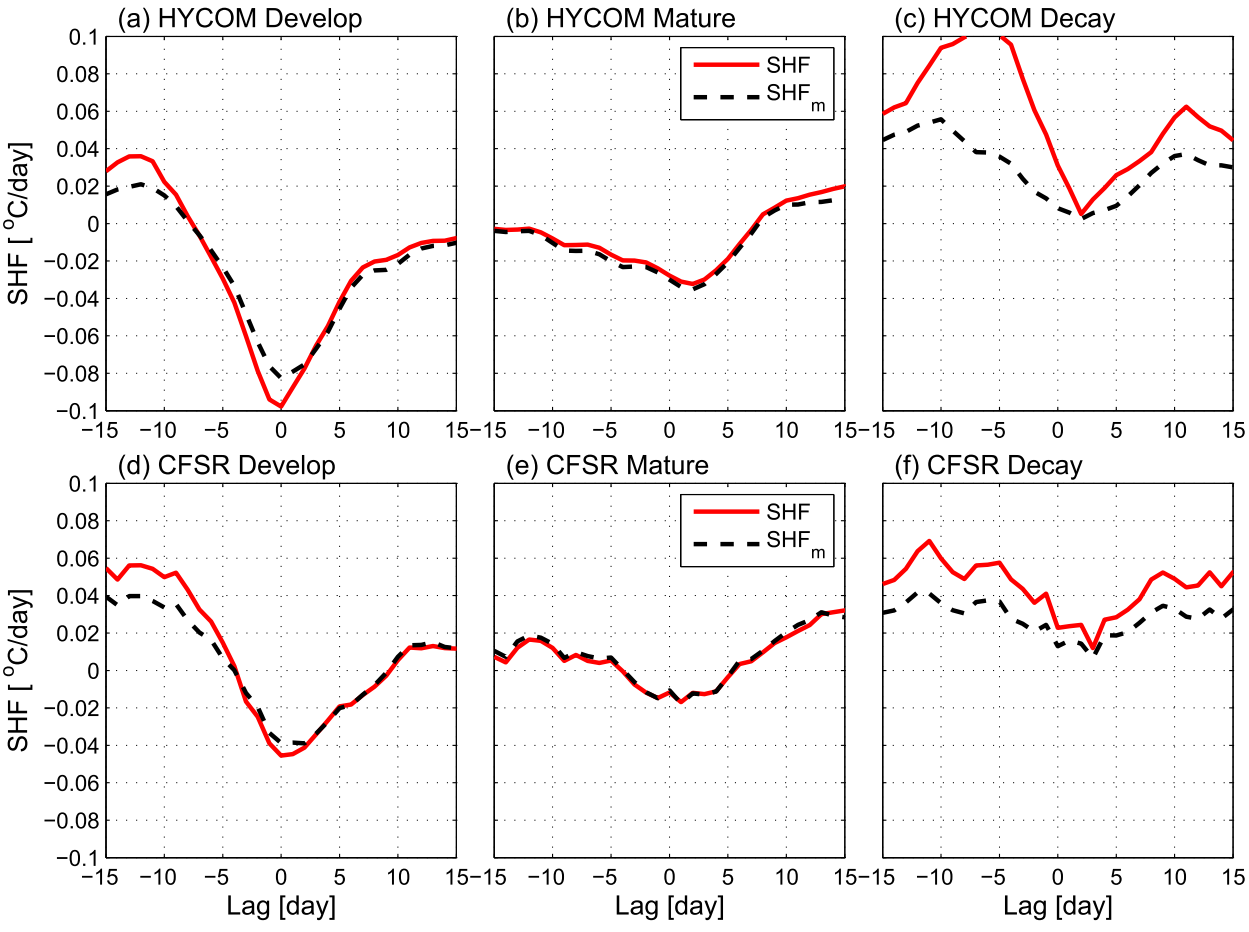

FIG. 12. Comparisons between surface heat flux forcing term (SHF; solid red) and the surface heat flux forcing term computed with ISM seasonal mean MLD (SHF_m; dashed black) for the composite MISO averaged over the EAS box from HYCOM MR for the (a) developing stage, (b) mature stage, and (c) decaying stage; (d)–(f) as in (a)–(c), but from CFSR data.

larger enhancement in the pre-event period. Similar analysis is performed using CFSR data, and the results are consistent with those from HYCOM, although the MLD effect is smaller in CFSR (Figs. 12d–f). These results demonstrate that seasonal variation of the MLD in the EAS has a significant impact on intraseasonal SST variability during MISOs. The shallow MLD in the developing and decaying stages of the ISM enhances the SST response to the MISO's heat flux forcing.

To further confirm our above analyses from HYCOM experiments and CFSR data, we examine the response of intraseasonal SST to intraseasonal heat flux forcing of MISOs using observational data (Fig. 13a). Here SST anomaly is taken 8 days after the date of Q_{net} anomaly, according to the observed phase relationship in Fig. 5c. For comparison, data points from the developing, mature, and decaying stages of the ISM are plotted in blue, red, and green colors, respectively. Data points from the developing stage tend to have much larger Q_{net} and SST anomalies than the others, reflecting the enhanced MISO intensity as revealed by our above analysis. Note that Q_{net} anomalies from the mature stage are larger than those from the decaying stage, but their corresponding SST anomalies are of similar magnitudes, indicating a more active response of SST to precipitation in the decaying stage. To better quantify the response rate, we perform a linear regression for the data points of each stage (straight lines in Fig. 13a). The decaying stage has the largest regression ratio of 0.085°C $(W m^{-2})^{-1}$, followed by the developing stage [0.071°C $(W m^{-2})^{-1}$], and the mature stage has the smallest [0.064°C $(W m^{-2})^{-1}$]. This result is consistent with Fig. 12, confirming that the shallow (deep) MLD in developing or decaying (mature) stage of the ISM amplifies (attenuates) the SST response to atmospheric forcing. One may wonder why the SST response is slightly more efficient in the decaying stage than in the developing stage, given that the mean MLD values are rather close for the two stages (Fig. 7a). The overall larger ratio for the decaying stage is partly attributed to the extremely shallow MLD along the western coast of India

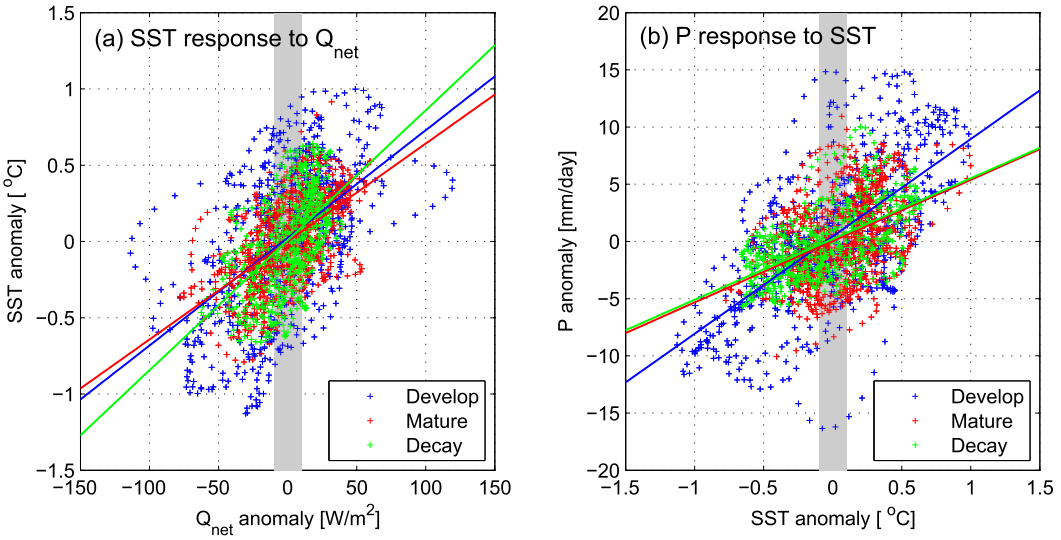

FIG. 13. (a) Scatterplot of 20–90-day surface net heat flux Q_{net} vs 20–90-day TMI SST for the developing (blue), mature (red), and decaying (green) stages of the ISM season. SST is taken 8 days after precipitation to measure SST response to Q_{net}. The straight lines are linear fittings using the data points with Q_{net} anomaly greater than 10 W m^{-2} (outside the gray shading). (b) As in (a), but to show TRMM precipitation response to SST. Precipitation is taken 6 days after SST, and the linear fittings are computed for data points with SST anomaly greater than 0.1°C.

during September–October (<20 m; Fig. 6). Data points in that area tend to have large SST and precipitation anomalies (Fig. 2) and thus largely weighted in the linear regression.

Although the SST response to precipitation is most efficient in the decaying stage, the overall MISO intensity is largest in the developing stage. Since the observed MISO variability is the manifestation of the two-way interaction between the ocean and atmosphere, the response of atmospheric convection to SST should also be examined. Based on Fig. 5c, the precipitation anomaly 6 days later is considered as a response to SST forcing (Fig. 13b). The precipitation-to-SST ratio is significantly larger in the developing stage than in the other two, indicating a more efficient response of atmospheric convection to SST forcing. This is probably due to the higher background SST (>29°C) in the developing stage (Figs. 6 and 7). Under such high SST condition, a relatively small change in SST may induce prominent perturbation in atmospheric convection. Regarding the impact of SST on convection, early studies showed that when SST exceeds 28°C, it ceases to be an important factor in determining convection variability (Gadgil et al. 1984; Graham and Barnett 1987). However, these studies were based on monthly observational data and did not take into account the temporal lag between SST and precipitation. Roxy (2014) revisited the SST–convection relationship with daily observational data and showed that in the ISM region the upper threshold for the SST–convection covariance is 31°C. It means that between 28° and 31°C SST is still an important factor in determining convection variability. This conclusion is also supported by studies with other data sources (Nair and Rajeev 2014). Nevertheless, the results in Fig. 13 clearly suggest the impact of the ocean state on the MISO intensity. While the MLD determines the amplitude of SST response to atmospheric forcing, the background SST can affect the response of atmospheric convection to the underlying SST forcing. Particularly, in the developing stage of the ISM, the shallow MLD and high SST in the EAS favor active two-way interaction between the ocean and atmosphere and thereby result in enhanced MISO intensity. As suggested by these results, the MISO variability is strongly dependent on air–sea interaction and the background ocean state. It is justified to say that the ocean, especially the Arabian Sea, plays an active role in the mechanisms of the MISO.

5. Summary and discussion

The northward-propagating MISOs in the tropical Indian Ocean are closely related to the active/break spells, interannual variability, and predictability of the ISM rainfall. Recognizing the importance of air–sea interaction in the MISO mechanisms, recent research tends to consider the MISO a coupled variability mode between the tropical ocean and atmosphere. Understanding SST variability and air–sea interaction processes at the intraseasonal time scale is helpful for integrating our knowledge of the MISO dynamics and

improving the model prediction of the ISM rainfall. In this study we investigate the intraseasonal precipitation and SST variability in the Arabian Sea associated with the MISOs, using satellite observations and the NCEP CFSR product. Some unique characteristics in the Arabian Sea are revealed, and the underlying physical processes are explored using an OGCM. The primary findings of the study are summarized below.

1) During the ISM season (15 May–15 October), the northward-propagating MISOs induce prominent SST and precipitation variations at 20–90-day time scale in the EAS and BoB regions, with STDs exceeding 9 mm day^{-1} in precipitation and 0.4°C in SST. In the EAS, MISOs propagate northward from the equator to southeast India at a mean speed of ~1.5 m s^{-1} (~1.18° latitude day^{-1}). Anomalies of precipitation and SST show a quadrature phase relationship. The rainfall peak occurs ~6 days after the warm SST anomaly, with a cold SST anomaly occurring ~9 days after the rainfall, indicative of swift response of atmospheric convection to SST anomaly and active role played by the ocean in the MISO mechanisms.
2) The CFSR product can reasonably represent precipitation variations of MISOs in both magnitude and spatiotemporal structure, but its SST anomalies are weaker by ~50% than TMI data. The SST–precipitation relationship in CFSR is also biased, showing quicker SST response to the atmospheric forcing of the MISO and slower precipitation response to SST anomaly.
3) MISOs in the EAS also exhibit clear intensity variation among the three stages of the ISM. They are strongest in the developing stage (15 May–30 June), followed by the decaying stage (1 September–15 October), and weakest in the mature stage (1 July–31 August). The Arabian Sea has a shallow MLD (<40 m) and a high SST (>29°C) in the ISM developing stage, which is a plausible cause for the intensification of the MISOs.
4) The observed intraseasonal SST variability and oceanic seasonal variations in the EAS are faithfully simulated by HYCOM. Parallel experiments of HYCOM are performed to explore the causes of intraseasonal SST variability. In the EAS, MISOs induce intraseasonal SST primarily through three major effects: SWR effects, wind speed–controlled Q_T (wind speed effect), and wind stress–driven oceanic processes (wind stress effect). Contributions from the three effects on the total SST anomaly are comparable, with the wind speed effect slightly larger than the other two. A mixed layer heat budget analysis for the EAS region reveals that SST anomalies are primarily induced by surface heat flux forcing (SHF) and to a much lesser degree by wind stress–driven mixed layer entrainment (ENT). However, the magnitude of SHF is determined by both wind stress–controlled MLD and total heat flux Q, which is contributed by SWR and Q_T.
5) Seasonal variations of MLD affect intraseasonal SST variability by changing the magnitude of SHF. The shallow MLD (<40 m) in developing and decaying stages increases the SHF magnitude and thereby enhances the SST response to the MISO's heat flux forcing. On the other hand, the higher mean SST in the developing stage (>29°C) leads to stronger response of MISO convection to SST forcing. Therefore, the ocean background state in the ISM developing stage, with shallow MLD and high SST, is favorable for active two-way air–sea interaction and the development of the first-pulse MISO event. These results provide compelling evidence for the vital role played by the ocean in the MISO mechanisms and have important implications for understanding and forecasting the ISM onset.

This research provides implications for the model simulation and forecast of MISOs from the oceanic point of view. The initial condition is critically important for ISM rainfall prediction, particularly for the extended prediction range. In the retrospective and operational forecasts of the CFSv2, CFSR is used as the initial condition. As a new-generation, state-of-the-art climate reanalysis product, CFSR achieves encouraging progress in improving the precipitation variability of MISOs comparing to the earlier versions. SST variability of the MISO, however, remains considerably underestimated, and the SST–precipitation phase relationship is severely biased. Given the importance of air–sea interaction in the MISO mechanisms, the biased intraseasonal SST in the initial state may cause large errors in the CFSv2 forecast. Wang et al. (2009) showed that the intensity and northward propagation behaviors of MISOs are quite sensitive to the amplitude of the underlying intraseasonal SST. When the prescribed SST variations were artificially raised to the magnitude of the observed skin temperature, GCMs were able to produce much more realistic MISO signals in precipitation and winds.

The underestimation of SST variability in CFSR may be partly attributable to the coarse vertical resolution of its ocean component (MOM4) near the sea surface. The top-layer thickness of the MOM4 is 10 m, which produces much smaller first-guess SST variability than skin temperature. Our HYCOM simulation, although without data assimilation or interactive air–sea coupling, produces stronger and more realistic temperature anomalies in the 2.6-m top layer (e.g., Figs. 9 and 10).

Intraseasonal temperature variability averaged over 0–10 m of HYCOM is weaker by ~3% than the top-layer temperature. Realistic representation of the observed skin temperature variability requires a finer vertical resolution to resolve the near-surface stratification and diurnal cycle (e.g., Shinoda 2005; Bernie et al. 2007; Y. Li et al. 2013) or a parameterization for the skin layer (e.g., Soloviev and Schlussel 1994). In addition, the underestimated SST variability can also result from errors in surface heat fluxes. Figure 5 suggests that surface SWR anomaly in CFSR is significantly weaker than in satellite observation. However, more specific suggestions for improving the MISO representation of CFSR and CFSv2 require a systematic inspection for the MOM4 component to identify the oceanic processes that are not adequately simulated or parameterized under the present model configuration, and this is the theme of our ongoing research.

The large impact of the oceanic background state, such as the seasonal evolution of SST and MLD, on the MISOs is clearly demonstrated by our results. Their realistic simulations are necessary for properly reproducing the air–sea interaction processes involved in the MISO. Roxy et al. (2013) suggested that the biases in seasonal MLD are a cause for the errors in the MISO forecast of the CFSv2. Duncan and Han (2009) argued that the presence of the salt-stratified barrier layer (Vinayachandran et al. 2002) during the ISM can affect intraseasonal SST variability of MISOs. The upper-ocean structure of the tropical Indian Ocean is rather complicated, making the realistic simulation a challenging task for existing ocean and coupled GCMs. For instance, MLD of the EAS region is thicker in CFSR than in Argo observations by ~5 m during the developing stage (Fig. 7a), which could be another cause for the underestimated variability in the first-guess SST variability of CFSR. Our HYCOM produces much thicker MLD than observations in the BoB (e.g., Li et al. 2014, 2015), which is likely a common bias among GCM simulations (e.g., Duncan and Han 2009; Akhil et al. 2014; Felton et al. 2014) and also seen in CFSR (Fig. 7b). Finer vertical resolution is again suggested to resolve the salt stratification in the BoB (Felton et al. 2014). In addition, most existing GCM simulations, including our HYCOM experiment and the MOM4 of CFSv2, use *K*-profile parameterization (KPP; Large et al. 1994) as the vertical mixing scheme. Whether the modeled mixed layer is sensitive to the choice of mixing scheme or related parameters is worthy of examination.

In this study we focused on examining the impact of the seasonal ocean variation on intraseasonal air–sea interaction of the MISO. As shown in Fig. 7, interannual variability of MLD is much weaker than its seasonal variability in the EAS and BoB. Nevertheless, under the strong influence of climate variability modes, SST of the tropical Indian Ocean exhibits pronounced variations over interannual, decadal, and multidecadal time scales (e.g., Saji et al. 1999; Webster et al. 1999; Izumo et al. 2008; Han et al. 2014; Roxy et al. 2014), which may also affect the MISO intensity by affecting the sensitivity of MISO convection to SST forcing. Given the vital role of the ocean in the MISO dynamics and the importance of the ISM onset to the economy and social structure of India, more attention and effort should be paid to understand oceanic processes in the tropical Indian Ocean and incorporate the knowledge into the monsoon prediction.

Acknowledgments. The authors gratefully acknowledge the financial support given by the Earth System Science Organization, Ministry of Earth Sciences, Government of India (Grant SSC-03-002; Project MM/SERP/CNRS/2013/INT-10/002), to conduct this research under Monsoon Mission. The research is also supported by NASA Ocean Vector Wind Science Team Award NNX14AM68G. Two anonymous reviewers provided helpful comments for improving the manuscript. We appreciate the National Center for Atmospheric Research (NCAR) CISL and the Office of Information Technology (OIT) of University of Colorado for providing and maintaining the computational resource. CFSR data are provided by NOMADS (http://nomads.ncdc.noaa.gov/) and NCAR (http://rda.ucar.edu/pub/cfsr.html); TRMM TMPA level 3B42 precipitation product is available online (http://mirador.gsfc.nasa.gov/); TRMM TMI SST product was downloaded from the TMI website (http://www.remss.com/missions/tmi); CCMP sea surface wind data were downloaded from NASA (http://podaac.jpl.nasa.gov/); CERES radiation data are taken from their website (http://ceres.larc.nasa.gov/); OAFlux latent and turbulent heat fluxes are provided by Dr. Lisan Yu (http://oaflux.whoi.edu/); gridded Argo in situ observational data are provided by Dr. Shigeki Hosoda (ftp://ftp2.jamstec.go.jp/pub/argo/MOAA_GPV/); and data processing and graphing work in this study are finished using a licensed Matlab program.

REFERENCES

Abhilash, S., and Coauthors, 2014: Prediction and monitoring of monsoon intraseasonal oscillations over Indian monsoon region in an ensemble prediction system using CFSv2. *Climate Dyn.*, **42**, 2801–2815, doi:10.1007/s00382-013-2045-9.

Achuthavarier, D., and V. Krishnamurthy, 2011: Role of Indian and Pacific SST in Indian summer monsoon intraseasonal variability. *J. Climate*, **24**, 2915–2930, doi:10.1175/2010JCLI3639.1.

Akhil, V. P., and Coauthors, 2014: A modeling study of the processes of surface salinity seasonal cycle in the Bay of Bengal. *J. Geophys. Res. Oceans*, **119**, 3926–3947, doi:10.1002/2013JC009632.

Alessandri, A., A. Borrelli, A. Cherchi, S. Materia, A. Navarra, J.-Y. Lee, and B. Wang, 2015: Prediction of Indian summer monsoon onset using dynamical subseasonal forecasts: Effects of realistic initialization of the atmosphere. *Mon. Wea. Rev.*, **143**, 778–793, doi:10.1175/MWR-D-14-00187.1.

Annamalai, H., and M. J. Slingo, 2001: Active/break cycles: Diagnosis of the intraseasonal variability of the Asian summer monsoon. *Climate Dyn.*, **18**, 85–102, doi:10.1007/s003820100161.

Atlas, R., J. Ardizzone, and R. N. Hoffman, 2008: Application of satellite surface wind data to ocean wind analysis. *Remote Sensing System Engineering*, P. Ardanuy and J. Puschell, Eds., International Society for Optical Engineering (SPIE Proceedings, Vol. 7087), 70870B, doi:10.1117/12.795371.

Bernie, D., E. Guilyardi, G. Madec, J. Slingo, and S. Woolnough, 2007: Impact of resolving the diurnal cycle in an ocean–atmosphere GCM. Part 1: A diurnally forced OGCM. *Climate Dyn.*, **29**, 575–590, doi:10.1007/s00382-007-0249-6.

Chatterjee, P., and B. N. Goswami, 2004: Structure, genesis and scale selection of the tropical quasi-biweekly mode. *Quart. J. Roy. Meteor. Soc.*, **130**, 1171–1194, doi:10.1256/qj.03.133.

Dai, A., T. Qian, K. E. Trenberth, and J. D. Milliman, 2009: Changes in continental freshwater discharge from 1948 to 2004. *J. Climate*, **22**, 2773–2792, doi:10.1175/2008JCLI2592.1.

de Boyer Montégut, C., J. Mignot, A. Lazar, and S. Cravatte, 2007: Control of salinity on the mixed layer depth in the world ocean: 1. General description. *J. Geophys. Res.*, **112**, C06011, doi:10.1029/2006JC003953.

Dee, D., and Coauthors, 2011: The ERA-Interim reanalysis: Configuration and performance of the data assimilation system. *Quart. J. Roy. Meteor. Soc.*, **137**, 553–597, doi:10.1002/qj.828.

Drbohlav, H.-K. L., and B. Wang, 2005: Mechanism of the northward-propagating intraseasonal oscillation: Insights from a zonally symmetric model. *J. Climate*, **18**, 952–972, doi:10.1175/JCLI3306.1.

Duchon, C. E., 1979: Lanczos filtering in one and two dimensions. *J. App. Meteor.*, **18**, 1016–1022, doi:10.1175/1520-0450(1979)018<1016:LFIOAT>2.0.CO;2.

Duncan, B., and W. Han, 2009: Indian Ocean intraseasonal sea surface temperature variability during boreal summer: Madden-Julian oscillation versus submonthly forcing and processes. *J. Geophys. Res.*, **114**, C05002, doi:10.1029/2008JC004958.

Felton, C. S., B. Subrahmanyam, V. S. N. Murty, and J. F. Shriver, 2014: Estimation of the barrier layer thickness in the Indian Ocean using Aquarius salinity. *J. Geophys. Res. Oceans*, **119**, 4200–4213, doi:10.1002/2013JC009759.

Fu, X., and B. Wang, 2004: Differences of boreal summer intraseasonal oscillations simulated in an atmosphere–ocean coupled model and an atmosphere-only model. *J. Climate*, **17**, 1263–1271, doi:10.1175/1520-0442(2004)017<1263:DOBSIO>2.0.CO;2.

——, ——, and T. Li, 2002: Impacts of air–sea coupling on the simulation of mean Asian summer monsoon in the ECHAM4 model. *Mon. Wea. Rev.*, **130**, 2889–2904, doi:10.1175/1520-0493(2002)130<2889:IOASCO>2.0.CO;2.

——, ——, ——, and J. P. McCreary, 2003: Coupling between northward-propagating, intraseasonal oscillations and sea surface temperature in the Indian Ocean. *J. Atmos. Sci.*, **60**, 1733–1753, doi:10.1175/1520-0469(2003)060<1733:CBNIOA>2.0.CO;2.

——, ——, D. E. Waliser, and L. Tao, 2007: Impact of atmosphere–ocean coupling on the predictability of monsoon intraseasonal oscillations. *J. Atmos. Sci.*, **64**, 157–174, doi:10.1175/JAS3830.1.

——, B. Yang, Q. Bao, and B. Wang, 2008: Sea surface temperature feedback extends the predictability of tropical intraseasonal oscillation. *Mon. Wea. Rev.*, **136**, 577–597, doi:10.1175/2007MWR2172.1.

Gadgil, S., and K. Rupa Kumar, 2006: The Asian monsoon—Agriculture and economy. *The Asian Monsoon*, B. Wang, Ed., Springer, 651–683.

——, N. Joshi, and P. Joseph, 1984: Ocean–atmosphere coupling over monsoon regions. *Nature*, **312**, 141–143, doi:10.1038/312141a0.

Goswami, B. B., R. P. M. Krishna, P. Mukhopadhyay, M. Khairoutdinov, and B. N. Goswami, 2015: Simulation of the Indian summer monsoon in the superparameterized Climate Forecast System version 2: Preliminary results. *J. Climate*, **28**, 8988–9012, doi:10.1175/JCLI-D-14-00607.1.

Goswami, B. N., 2005: South Asian monsoon. *Intraseasonal Variability in the Atmosphere-Ocean Climate System*, W. Lau and D. Waliser, Eds., Springer, 19–61.

——, and R. S. Ajaya Mohan, 2001: Intraseasonal oscillations and interannual variability of the Indian summer monsoon. *J. Climate*, **14**, 1180–1198, doi:10.1175/1520-0442(2001)014<1180:IOAIVO>2.0.CO;2.

——, G. Wu, and T. Yasunari, 2006: The annual cycle, intraseasonal oscillations, and roadblock to seasonal predictability of the Asian summer monsoon. *J. Climate*, **19**, 5078–5099, doi:10.1175/JCLI3901.1.

Goswami, P., and K. C. Gouda, 2009: Comparative evaluation of two ensembles for long-range forecasting of monsoon rainfall. *Mon. Wea. Rev.*, **137**, 2893–2907, doi:10.1175/2009MWR2767.1.

Graham, N., and T. Barnett, 1987: Sea surface temperature, surface wind divergence, and convection over tropical oceans. *Science*, **238**, 657–659, doi:10.1126/science.238.4827.657.

Halliwell, G. R., 2004: Evaluation of vertical coordinate and vertical mixing algorithms in the Hybrid-Coordinate Ocean Model (HYCOM). *Ocean Modell.*, **7**, 285–322, doi:10.1016/j.ocemod.2003.10.002.

Han, W., J. Vialard, M. J. McPhaden, T. Lee, Y. Masumoto, M. Feng, and W. P. M. de Ruijter, 2014: Indian Ocean decadal variability: A review. *Bull. Amer. Meteor. Soc.*, **95**, 1679–1703, doi:10.1175/BAMS-D-13-00028.1.

Harrison, D., and G. A. Vecchi, 2001: January 1999 Indian Ocean cooling event. *Geophys. Res. Lett.*, **28**, 3717–3720, doi:10.1029/2001GL013506.

Hosoda, S., T. Ohira, and T. Nakamura, 2008: A monthly mean dataset of global oceanic temperature and salinity derived from Argo float observations. *JAMSTEC Rep. Res. Dev.*, **8**, 47–59.

Hoyos, C. D., and P. J. Webster, 2007: The role of intraseasonal variability in the nature of Asian monsoon precipitation. *J. Climate*, **20**, 4402–4424, doi:10.1175/JCLI4252.1.

Huffman, G. J., and Coauthors, 2007: The TRMM Multisatellite Precipitation Analysis (TMPA): Quasi-global, multiyear, combined-sensor precipitation estimates at fine scales. *J. Hydrometeor.*, **8**, 38–55, doi:10.1175/JHM560.1.

Izumo, T., C. B. Montégut, J.-J. Luo, S. K. Behera, S. Masson, and T. Yamagata, 2008: The role of the western Arabian Sea

upwelling in Indian monsoon rainfall variability. *J. Climate*, **21**, 5603–5623, doi:10.1175/2008JCLI2158.1.

Jiang, X., T. Li, and B. Wang, 2004: Structures and mechanisms of the northward propagating boreal summer intraseasonal oscillation. *J. Climate*, **17**, 1022–1039, doi:10.1175/1520-0442(2004)017<1022:SAMOTN>2.0.CO;2.

Jochum, M., and R. Murtugudde, 2005: Internal variability of Indian Ocean SST. *J. Climate*, **18**, 3726–3738, doi:10.1175/JCLI3488.1.

Joseph, P. V., and T. P. Sabin, 2008: An ocean–atmosphere interaction mechanism for the active break cycle of the Asian summer monsoon. *Climate Dyn.*, **30**, 553–566, doi:10.1007/s00382-007-0305-2.

——, J. K. Eischeid, and R. J. Pyle, 1994: Interannual variability of the onset of the Indian summer monsoon and its association with atmospheric features, El Niño, and sea surface temperature anomalies. *J. Climate*, **7**, 81–105, doi:10.1175/1520-0442(1994)007<0081:IVOTOO>2.0.CO;2.

Kara, A. B., H. E. Hurlburt, and A. J. Wallcraft, 2005: Stability-dependent exchange coefficients for air–sea fluxes. *J. Atmos. Oceanic Technol.*, **22**, 1080–1094, doi:10.1175/JTECH1747.1.

Keerthi, M., M. Lengaigne, J. Vialard, C. de Boyer Montégut, and P. Muraleedharan, 2013: Interannual variability of the tropical Indian Ocean mixed layer depth. *Climate Dyn.*, **40**, 743–759, doi:10.1007/s00382-012-1295-2.

Kemball-Cook, S., and B. Wang, 2001: Equatorial waves and air–sea interaction in the boreal summer intraseasonal oscillation. *J. Climate*, **14**, 2923–2942, doi:10.1175/1520-0442(2001)014<2923:EWAASI>2.0.CO;2.

Kiladis, G. N., and K. M. Weickmann, 1997: Horizontal structure and seasonality of large-scale circulations associated with submonthly tropical convection. *Mon. Wea. Rev.*, **125**, 1997–2013, doi:10.1175/1520-0493(1997)125<1997:HSASOL>2.0.CO;2.

Krishnamurti, T. N., and P. Ardanuy, 1980: The 10 to 20-day westward propagating mode and "breaks in the monsoons." *Tellus*, **32A**, 15–26, doi:10.1111/j.2153-3490.1980.tb01717.x.

Large, W. G., J. C. McWilliams, and S. C. Doney, 1994: Oceanic vertical mixing: A review and a model with a nonlocal boundary layer parameterization. *Rev. Geophys.*, **32**, 363–403, doi:10.1029/94RG01872.

Lau, K. M., and P. H. Chan, 1985: Aspects of the 40–50 day oscillation during the northern winter as inferred from outgoing longwave radiation. *Mon. Wea. Rev.*, **113**, 1889–1909, doi:10.1175/1520-0493(1985)113<1889:AOTDOD>2.0.CO;2.

——, and S. Yang, 1996: Seasonal variation, abrupt transition, and intraseasonal variability associated with the Asian summer monsoon in the GLA GCM. *J. Climate*, **9**, 965–985, doi:10.1175/1520-0442(1996)009<0965:SVATAI>2.0.CO;2.

Lawrence, D. M., and P. J. Webster, 2002: The boreal summer intraseasonal oscillation: Relationship between northward and eastward movement of convection. *J. Atmos. Sci.*, **59**, 1593–1606, doi:10.1175/1520-0469(2002)059<1593:TBSIOR>2.0.CO;2.

Li, K., W. Yu, T. Li, V. S. N. Murty, S. Khokiattiwong, T. R. Adi, and S. Budi, 2013: Structures and mechanisms of the first-branch northward-propagating intraseasonal oscillation over the tropical Indian Ocean. *Climate Dyn.*, **40**, 1707–1720, doi:10.1007/s00382-012-1492-z.

Li, Y., W. Han, T. Shinoda, C. Wang, R. C. Lien, J. N. Moum, and J. W. Wang, 2013: Effects of the diurnal cycle in solar radiation on the tropical Indian Ocean mixed layer variability during wintertime Madden-Julian oscillations. *J. Geophys. Res. Oceans*, **118**, 4945–4964, doi:10.1002/jgrc.20395.

——, ——, ——, ——, M. Ravichandran, and J.-W. Wang, 2014: Revisiting the wintertime intraseasonal SST variability in the tropical south Indian Ocean: Impact of the ocean interannual variation. *J. Phys. Oceanogr.*, **44**, 1886–1907, doi:10.1175/JPO-D-13-0238.1.

——, ——, and T. Lee, 2015: Intraseasonal sea surface salinity variability in the equatorial Indo-Pacific Ocean induced by Madden-Julian oscillations. *J. Geophys. Res. Oceans*, **120**, 2233–2258, doi:10.1002/2014JC010647.

Loeb, N. G., K. J. Priestley, D. P. Kratz, E. B. Geier, R. N. Green, B. A. Wielicki, P. O. R. Hinton, and S. K. Nolan, 2001: Determination of unfiltered radiances from the Clouds and the Earth's Radiant Energy System instrument. *J. Appl. Meteor.*, **40**, 822–835, doi:10.1175/1520-0450(2001)040<0822:DOURFT>2.0.CO;2.

Madden, R. A., and P. R. Julian, 1971: Detection of a 40–50 day oscillation in the zonal wind in the tropical Pacific. *J. Atmos. Sci.*, **28**, 702–708, doi:10.1175/1520-0469(1971)028<0702:DOADOI>2.0.CO;2.

Murtugudde, R., R. Seager, and P. Thoppil, 2007: Arabian Sea response to monsoon variations. *Paleoceanography*, **22**, PA4217, doi:10.1029/2007PA001467.

Nair, A. K. M., and K. Rajeev, 2014: Multiyear *CloudSat* and *CALIPSO* observations of the dependence of cloud vertical distribution on sea surface temperature and tropospheric dynamics. *J. Climate*, **27**, 672–683, doi:10.1175/JCLI-D-13-00062.1.

Ninomiya, K., and C. Kobayashi, 1999: Precipitation and moisture balance of the Asian summer monsoon in 1991. Part II: Moisture transport and moisture balance. *J. Meteor. Soc. Japan*, **77**, 77–99.

Papa, F., F. Durand, W. B. Rossow, A. Rahman, and S. K. Bala, 2010: Satellite altimeter-derived monthly discharge of the Ganga-Brahmaputra River and its seasonal to interannual variations from 1993 to 2008. *J. Geophys. Res.*, **115**, C12013, doi:10.1029/2009JC006075.

Pegion, K., and B. P. Kirtman, 2008: The impact of air–sea interactions on the simulation of tropical intraseasonal variability. *J. Climate*, **21**, 6616–6635, doi:10.1175/2008JCLI2209.1.

Prodhomme, C., P. Terray, S. Masson, G. Boschat, and T. Izumo, 2015: Oceanic factors controlling the Indian summer monsoon onset in a coupled model. *Climate Dyn.*, **44**, 977–1002, doi:10.1007/s00382-014-2200-y.

Qi, Y., R. Zhang, T. Li, and M. Wen, 2008: Interactions between the summer mean monsoon and the intraseasonal oscillation in the Indian monsoon region. *Geophys. Res. Lett.*, **35**, L17704, doi:10.1029/2008GL034517.

Rajeevan, M., S. Gadgil, and J. Bhate, 2010: Active and break spells of the Indian summer monsoon. *J. Earth Syst. Sci.*, **119**, 229–247, doi:10.1007/s12040-010-0019-4.

Rajendran, K., and A. Kitoh, 2006: Modulation of tropical intraseasonal oscillations by ocean–atmosphere coupling. *J. Climate*, **19**, 366–391, doi:10.1175/JCLI3638.1.

Rao, R. R., and R. Sivakumar, 1999: On the possible mechanisms of the evolution of a mini-warm pool during the pre-summer monsoon season and the genesis of onset vortex in the south-eastern Arabian Sea. *Quart. J. Roy. Meteor. Soc.*, **125**, 787–809, doi:10.1002/qj.49712555503.

Reynolds, R. W., T. M. Smith, C. Liu, D. B. Chelton, K. S. Casey, and M. G. Schlax, 2007: Daily high-resolution-blended analyses for sea surface temperature. *J. Climate*, **20**, 5473–5496, doi:10.1175/2007JCLI1824.1.

Roxy, M., 2014: Sensitivity of precipitation to sea surface temperature over the tropical summer monsoon region—and its quantification. *Climate Dyn.*, **43**, 1159–1169, doi:10.1007/s00382-013-1881-y.

——, and Y. Tanimoto, 2007: Role of SST over the Indian Ocean in influencing the intraseasonal variability of the Indian summer monsoon. *J. Meteor. Soc. Japan*, **85**, 349–358, doi:10.2151/jmsj.85.349.

——, and ——, 2012: Influence of sea surface temperature on the intraseasonal variability of the South China Sea summer monsoon. *Climate Dyn.*, **39**, 1209–1218, doi:10.1007/s00382-011-1118-x.

——, ——, B. Preethi, P. Terray, and R. Krishnan, 2013: Intraseasonal SST-precipitation relationship and its spatial variability over the tropical summer monsoon region. *Climate Dyn.*, **41**, 45–61, doi:10.1007/s00382-012-1547-1.

——, K. Ritika, P. Terray, and S. Masson, 2014: The curious case of Indian Ocean warming. *J. Climate*, **27**, 8501–8509, doi:10.1175/JCLI-D-14-00471.1.

Sabeerali, C. T., S. A. Rao, G. George, D. N. Rao, S. Mahapatra, A. Kulkarni, and R. Murtugudde, 2014: Modulation of monsoon intraseasonal oscillations in the recent warming period. *J. Geophys. Res. Atmos.*, **119**, 5185–5203, doi:10.1002/2013JD021261.

Saha, S., and Coauthors, 2010: The NCEP Climate Forecast System Reanalysis. *Bull. Amer. Meteor. Soc.*, **91**, 1015–1057, doi:10.1175/2010BAMS3001.1.

——, and Coauthors, 2014: The NCEP Climate Forecast System version 2. *J. Climate*, **27**, 2185–2208, doi:10.1175/JCLI-D-12-00823.1.

Saji, N., B. Goswami, P. Vinayachandran, and T. Yamagata, 1999: A dipole mode in the tropical Indian Ocean. *Nature*, **401**, 360–363.

Sengupta, D., and M. Ravichandran, 2001: Oscillations of Bay of Bengal sea surface temperature during the 1998 summer monsoon. *Geophys. Res. Lett.*, **28**, 2033–2036, doi:10.1029/2000GL012548.

——, B. N. Goswami, and R. Senan, 2001: Coherent intraseasonal oscillations of ocean and atmosphere during the Asian summer monsoon. *Geophys. Res. Lett.*, **28**, 4127–4130, doi:10.1029/2001GL013587.

Seo, K.-H., J.-K. E. Schemm, W. Wang, and A. Kumar, 2007: The boreal summer intraseasonal oscillation simulated in the NCEP Climate Forecast System: The effect of sea surface temperature. *Mon. Wea. Rev.*, **135**, 1807–1827, doi:10.1175/MWR3369.1.

Sharmila, S., and Coauthors, 2013: Role of ocean–atmosphere interaction on northward propagation of Indian summer monsoon intra-seasonal oscillations (MISO). *Climate Dyn.*, **41**, 1651–1669, doi:10.1007/s00382-013-1854-1.

Shinoda, T., 2005: Impact of the diurnal cycle of solar radiation on intraseasonal SST variability in the western equatorial Pacific. *J. Climate*, **18**, 2628–2636, doi:10.1175/JCLI3432.1.

Shukla, J., 1975: Effect of Arabian Sea surface temperature anomaly on Indian summer monsoon: A numerical experiment with the GFDL model. *J. Atmos. Sci.*, **32**, 503–511, doi:10.1175/1520-0469(1975)032<0503:EOASST>2.0.CO;2.

Soloviev, A. V., and P. Schlussel, 1994: Parameterization of the cool skin of the ocean and of the air–ocean gas transfer on the basis of modeling surface renewal. *J. Phys. Oceanogr.*, **24**, 1339–1346, doi:10.1175/1520-0485(1994)024<1339:POTCSO>2.0.CO;2.

Stevenson, J. W., and P. P. Niiler, 1983: Upper ocean heat budget during the Hawaii-to-Tahiti shuttle experiment. *J. Phys. Oceanogr.*, **13**, 1894–1907, doi:10.1175/1520-0485(1983)013<1894:UOHBDT>2.0.CO;2.

Vialard, J., A. Jayakumar, C. Gnanaseelan, M. Lengaigne, D. Sengupta, and B. Goswami, 2012: Processes of 30–90 days sea surface temperature variability in the northern Indian Ocean during boreal summer. *Climate Dyn.*, **38**, 1901–1916, doi:10.1007/s00382-011-1015-3.

Vinayachandran, P. N., V. S. N. Murty, and V. Ramesh Babu, 2002: Observations of barrier layer formation in the Bay of Bengal during summer monsoon. *J. Geophys. Res.*, **107**, 8018, doi:10.1029/2001JC000831.

Waliser, D. E., N. E. Graham, and C. Gautier, 1993: Comparison of the highly reflective cloud and outgoing longwave radiation datasets for use in estimating tropical deep convection. *J. Climate*, **6**, 331–353, doi:10.1175/1520-0442(1993)006<0331:COTHRC>2.0.CO;2.

——, Z. Zhang, K. Lau, and J. H. Kim, 2001: Interannual sea surface temperature variability and the predictability of tropical intraseasonal variability. *J. Atmos. Sci.*, **58**, 2596–2615, doi:10.1175/1520-0469(2001)058<2596:ISSTVA>2.0.CO;2.

——, R. Murtugudde, and L. E. Lucas, 2004: Indo-Pacific Ocean response to atmospheric intraseasonal variability: 2. Boreal summer and the intraseasonal oscillation. *J. Geophys. Res.*, **109**, C03030, doi:10.1029/2003JC002002.

Wallcraft, A. J., E. J. Metzger, and S. N. Carroll, 2009: Software design description for the Hybrid Coordinate Ocean Model (HYCOM) version 2.2. Naval Research Laboratory Tech. Rep. NRL/MR/7320-09-9166, 155 pp. [Available online at https://hycom.org/attachments/063_metzger1-2009.pdf.]

Wang, B., and X. Xie, 1998: Coupled modes of the warm pool climate system. Part I: The role of air–sea interaction in maintaining Madden–Julian oscillation. *J. Climate*, **11**, 2116–2135, doi:10.1175/1520-0442-11.8.2116.

——, Q. Ding, X. Fu, I.-S. Kang, K. Jin, J. Shukla, and F. Doblas-Reyes, 2005: Fundamental challenge in simulation and prediction of summer monsoon rainfall. *Geophys. Res. Lett.*, **32**, L15711, doi:10.1029/2005GL022734.

Wang, J., W. Wang, X. Fu, and K.-H. Seo, 2012: Tropical intraseasonal rainfall variability in the CFSR. *Climate Dyn.*, **38**, 2191–2207, doi:10.1007/s00382-011-1087-0.

Wang, W., M. Chen, and A. Kumar, 2009: Impacts of ocean surface on the northward propagation of the boreal summer intraseasonal oscillation in the NCEP Climate Forecast System. *J. Climate*, **22**, 6561–6576, doi:10.1175/2009JCLI3007.1.

——, P. Xie, S.-H. Yoo, Y. Xue, A. Kumar, and X. Wu, 2011: An assessment of the surface climate in the NCEP Climate Forecast System Reanalysis. *Climate Dyn.*, **37**, 1601–1620, doi:10.1007/s00382-010-0935-7.

Webster, P. J., V. Magaña, T. Palmer, J. Shukla, R. Tomas, M. U. Yanai, and T. Yasunari, 1998: Monsoons: Processes, predictability, and the prospects for prediction. *J. Geophys. Res.*, **103**, 14 451–14 510, doi:10.1029/97JC02719.

——, A. M. Moore, J. P. Loschnigg, and R. R. Leben, 1999: Coupled ocean–atmosphere dynamics in the Indian Ocean during 1997–98. *Nature*, **401**, 356–360, doi:10.1038/43848.

——, and Coauthors, 2002: The JASMINE pilot study. *Bull. Amer. Meteor. Soc.*, **83**, 1603–1630, doi:10.1175/BAMS-83-11-1603.

Wentz, F. J., C. Gentemann, D. Smith, and D. Chelton, 2000: Satellite measurements of sea surface temperature through clouds. *Science*, **288**, 847–850, doi:10.1126/science.288.5467.847.

Wielicki, B. A., B. R. Barkstrom, E. F. Harrison, R. B. Lee III, G. Louis Smith, and J. E. Cooper, 1996: Clouds and the Earth's Radiant Energy System (CERES): An earth observing system experiment. *Bull. Amer. Meteor. Soc.*, **77**, 853–868, doi:10.1175/1520-0477(1996)077<0853:CATERE>2.0.CO;2.

Wu, R., and B. Wang, 2001: Multi-stage onset of the summer monsoon over the western North Pacific. *Climate Dyn.*, **17**, 277–289, doi:10.1007/s003820000118.

Xi, J., L. Zhou, R. Murtugudde, and L. Jiang, 2015: Impacts of intraseasonal SST anomalies on precipitation during Indian summer monsoon. *J. Climate*, **28**, 4561–4575, doi:10.1175/JCLI-D-14-00096.1.

Xue, Y., B. Huang, Z.-Z. Hu, A. Kumar, C. Wen, D. Behringer, and S. Nadiga, 2011: An assessment of oceanic variability in the NCEP Climate Forecast System Reanalysis. *Climate Dyn.*, **37**, 2511–2539, doi:10.1007/s00382-010-0954-4.

Yasunari, T., 1979: Cloudiness fluctuation associated with the Northern Hemisphere summer monsoon. *J. Meteor. Soc. Japan*, **57**, 227–242.

——, 1980: A quasi-stationary appearance of 30- to 40-day period in the cloudiness fluctuations during the summer monsoon over India. *J. Meteor. Soc. Japan*, **58**, 225–229.

Yu, L., and R. A. Weller, 2007: Objectively analyzed air–sea heat fluxes for the global ice-free oceans (1981–2005). *Bull. Amer. Meteor. Soc.*, **88**, 527–539, doi:10.1175/BAMS-88-4-527.

Zhang, C., 2005: Madden-Julian oscillation. *Rev. Geophys.*, **43**, RG2003, doi:10.1029/2004RG000158.

Zhou, L., and R. Murtugudde, 2014: Impact of northward-propagating intraseasonal variability on the onset of Indian summer monsoon. *J. Climate*, **27**, 126–139, doi:10.1175/JCLI-D-13-00214.1.